

Residual Study: Testing Jupiter Atmosphere Models Against Juno MWR Observations

Zhimeng Zhang¹, Virgil Adumitroaie³, Michael Allison⁸, John Arballo³, Sushil Atreya⁴, Gordon Bjoraker⁸, Scott Bolton², Shannon Brown³, Leigh N. Fletcher¹¹, Tristan Guillot⁷, Samuel Gulkis³, Amoree Hodges⁶, Andrew Ingersoll¹, Michael Janssen³, Steven Levin³, Cheng Li¹², Liming Li¹⁰, Jonathan Lunine⁵, Sidharth Misra³, Glenn Orton³, Fabiano Oyafuso³, Paul Steffes⁶, Michael H. Wong¹³

¹California Institute of Technology, Pasadena CA, 91125

²Southwest Research Institute, San Antonio TX, 78228

³Jet Propulsion Laboratory, California Institute of Technology, Pasadena CA, 91109

⁴University of Michigan, Ann Arbor MI, 48109

⁵Cornell University, Ithaca NY, 14850

⁶Georgia Institute of Technology, Atlanta GA, 30332

⁷Universite Cote d'Azur, COA, Lagrange CNRS, 06304 Nice, France

⁸Goddard Institute for Space Studies, New York NY, 10025

⁹Lockheed Martin, Grand Prairie TX, 75208

¹⁰University of Houston, Houston TX, 77004

¹¹School of Physics and Astronomy, University of Leicester, University Road, Leicester, LE1 7RH, United Kingdom.

¹²University of California, Berkeley

¹³SETI Institute, Mountain View CA 94043

Abstract

The Juno spacecraft provides unique close-up views of Jupiter underneath the synchrotron radiation belts while circling Jupiter in its 53-day orbits. The Microwave Radiometer (MWR) on board measures Jupiter thermal radiation at wavelengths between 1.37 cm and 50 cm, penetrating the atmosphere to a pressure of a few hundred bars and greater. The mission provides the first measurements of Jupiter's deep atmosphere, down to ~250 bars in pressure, constraining the vertical distributions of its kinetic temperature and constituents. As a result, vertical structure models of Jupiter's atmosphere may now be tested by comparison with MWR data. Taking into account the MWR beam patterns and observation geometries, we test several published Jupiter atmospheric models against MWR data. Our residual analysis confirms Li et al. 2017's result that ammonia depletion persists down to 50~60 bars where ground-based VLA was not able to observe. We also present an extension of the study that iteratively improves the input model and generates Jupiter brightness temperature maps which best match the MWR data. A feature of Juno's north-to-south scanning approach is that latitudinal structure is more easily obtained than longitudinal, and the creation of optimum two-dimensional maps is addressed in this approach.

This is the author manuscript accepted for publication and has undergone full peer review but has not been through the copyediting, typesetting, pagination and proofreading process, which may lead to differences between this version and the Version of Record. Please cite this article as:

Zhang et al. 2016, the Juno spacecraft started its flybys over Jupiter, allowing the Microwave Radiometer (MWR) instrument [Janssen et al. 2017] to measure the thermal emission of Jupiter's atmosphere from pressure levels of

46 approximately 0.5 bar to a few hundred bars [Bolton et al., 2017]. A main objective of the MWR is to measure
 47 Jupiter's deep water abundance, because it is key to understanding the history of the giant planet's volatile and
 48 heavy elements [Helled and Lunine, 2014], and is essential for understanding the meteorology that is observed at the
 49 visible cloud level [e.g. Showman, 2007]. Jupiter's brightness temperatures at the MWR wavelengths are highly
 50 sensitive to the ammonia distribution in Jupiter's atmosphere [Janssen et al., 2017]., the major opacity source in the
 51 MWR channels. Prior to the arrival of the Juno spacecraft, the only direct knowledge of Jupiter's deep atmosphere
 52 profile (i.e. temperature, water and ammonia abundances) came from the Galileo Probe, which was restricted to in
 53 situ measurements during a single plunge into the atmosphere at a longitude of 4.5°W (System III) and a
 54 planetocentric latitude of 6.5°N (within a relatively dry and cloudless area at the southern edge of the north
 55 equatorial belt, NEB) down to less than 20 bars. Most previous works have focused on similarly clear and dry down-
 56 welling regions with depletions of ammonia and water, where the probe entered and where spectroscopic
 57 measurements are taken [Bjoraker et al. 1986, Grassi et al. 2017]. Earth-based radio observations [e.g. de Pater et al.
 58 2016, 2019] give global coverage, but require assumptions about limb-darkening because viewing angle is
 59 correlated with latitude, and are limited by the foreground synchrotron radiation emitted by high-energy electrons
 60 gyrating around Jupiter's intense magnetic field [Burke and Franklin 1955, Santos-Costa et al. 2017]. Juno's orbit
 61 takes it beneath the radiation belts, largely alleviating the limitations imposed by synchrotron emission, and allowing
 62 finer spatial resolution than most Earth-based radio observations while observing each location from multiple
 63 viewing angles.

64
 65 Li et al. (2017) have retrieved a vertical ammonia distribution from 0.5 bar to 100 bars inverted from Juno MWR
 66 observations from Juno's first science pass, perijove (PJ) 1, and Li et al. (2020) used MWR data to derive water and
 67 ammonia abundance in a narrow latitude band near the equator. de Pater et al. (2019) also derived a vertical
 68 ammonia distribution from ground-based VLA observations at 3-37 GHz, showing compatibility with a subset of the
 69 MWR data described by Li et al. (2017). However, interpreting MWR data in this way requires complex data
 70 processing and a variety of assumptions about data smoothness, symmetry of the planet, etc. [see, e.g., Oyafuso et al
 71 2020]. Instead, in this paper we apply a model in the forward direction to produce synthetic MWR observations and
 72 then compare those predictions with the actual MWR data set. This approach is simpler, requires fewer assumptions,
 73 and allows direct comparison of residuals with the known uncertainties of the MWR data set [Janssen et al. 2017].
 74

75 In Section 2, we begin with a brief description of the MWR observations. In Section 3, we provide details of the
 76 modeling approach and present the iterative residual calculation used to generate 2D Jupiter maps with respect to
 77 latitude and longitude. In Section 4, we test several Jupiter atmosphere models proposed by previous works against
 78 the MWR observations.
 79

80 81 2. MWR Observation Description

82
 83 The Juno/MWR instrument measures the thermal emission of Jupiter's atmosphere at six widely separated
 84 wavelengths and multiple emission angles from nadir to greater than 50 degrees. The antenna temperature (T_a)
 85 represents the power received by the antenna, which is the convolution of the source brightness temperature (T_b)
 86 distribution in the field of view over the broad antenna gain pattern [Janssen et al. 2017]; i.e.,
 87

$$88 \quad T_a(\theta, \phi) = \int_0^{2\pi} \int_0^\pi T_b(\theta', \phi') g(\theta' - \theta, \phi' - \phi) \sin(\theta' - \theta) d\theta' d\phi' \quad (1)$$

89
 90 where $(\theta' - \theta, \phi' - \phi)$ is the angular deviation from the beam boresight direction (θ, ϕ) . $T_b(\theta', \phi')$ is the
 91 brightness temperature in the direction of the solid angle element $\sin(\theta' - \theta) d\theta' d\phi'$ and $g(\theta' - \theta, \phi' - \phi)$ is the
 92 gain of the antenna toward this direction for an antenna pointed in the direction (θ, ϕ) . The gain $g(\theta, \phi)$ [Janssen
 93 1993, Chapter 1, Eqn. 1.27] is normalized to 1 over the 4π sky as shown in Equation 2 [Janssen et al. 2017], which
 94 makes it a factor of 4π smaller than the commonly defined gain in radio astronomy [Rohlfs and Wilson 1999,
 95 Chapter 5, Eqn. 5.48].
 96
 97

$$98 \quad \int_0^{2\pi} \int_0^\pi g(\theta, \phi) \sin\theta d\theta d\phi = 1 \quad (2)$$

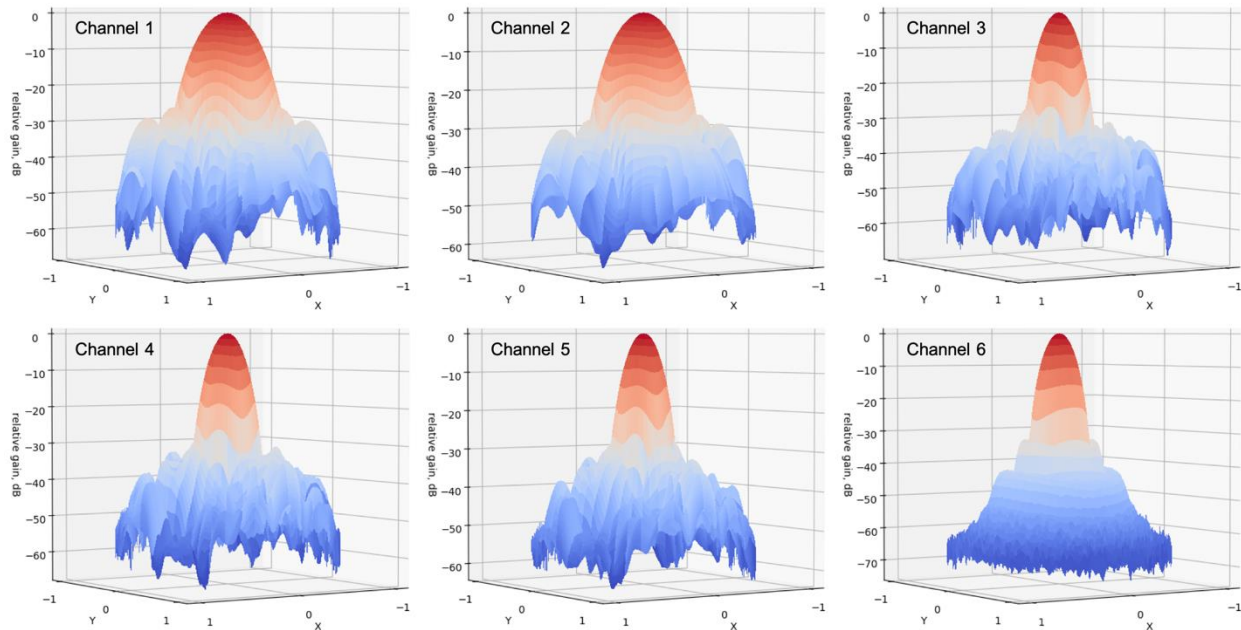
99

100 The main beam of the antenna contributes most to the antenna temperature and can be considered as a general
 101 estimate of the boresight antenna temperature at (θ, ϕ) ; however, the sidelobes view a brightness distribution that can
 102 be considerably different. For example, we need to account for off axis Jovian thermal emission at different
 103 emission angles, the empty-sky cosmic microwave background (CMB), galactic emission, and Jovian synchrotron
 104 radiation, the latter being especially significant in channels 1 and 2.
 105

106 The gain pattern for each of the six antennas has been measured over the full sphere pre-launch [Janssen et al., 2017]
 107 (see Figure 1 for antenna pattern, relative gain with respect to the peak gain). An arbitrary Jupiter atmosphere model
 108 can thus be used to calculate the antenna temperature at all positions on Jupiter from all viewing perspectives. This
 109 modeled antenna temperature can then be compared with observed antenna temperatures. The residual is defined as
 110 the difference between the two:
 111

$$T_{resid} = T_a^{obs} - T_a^{model} \quad (3)$$

114 The set of residuals obtained for a given pass is thus a measure of how consistent the model is with the real Jupiter
 115 atmosphere. Note also that the radiometric measurements have both systematic calibration uncertainties in addition
 116 to thermal measurement noise that must be taken into account, so that interpreting the residuals is not always as
 117 simple as minimizing the offset. If the model matched Jupiter exactly, the systematic measurement effect due to
 118 absolute calibration error could introduce constant but unknown offsets to all the residuals at each frequency. Brown
 119 et al. (2020) estimate this to be as large as 2%. Other calibration errors such as uncertainties in the measured beam
 120 patterns are expected to result in residuals of this order or less [Janssen et al, 2017]. Intrinsic receiver noise
 121 introduces variations of order 0.1% which leads to scatter in the residuals [Oyafuso et al. 2020]. In practice, an
 122 atmospheric model would be considered inconsistent with the MWR measurements if the bulk residuals are larger
 123 than 2%. It would also be considered inconsistent if the residuals for any channel varied by more than 0.2%.
 124



125 **Figure 1.** Antenna patterns (relative gain in dB with respect to peak gain) for all 6 MWR channels. The main beam
 126 half power width is 20° for channels 1 and 2, 12° for channels 3, 4, 5, and 11° for channel 6.
 127 $x = \sin(\text{polar angle}) * \cos(\text{azimuthal angle})$, $y = \sin(\text{polar angle}) * \sin(\text{azimuthal angle})$, where $x = y = 0$
 128 at the boresight.
 129

130
 131
 132 **3. Residual Analysis**
 133

134 We developed a residual analysis method to compare any brightness temperature distribution model over the planet
 135 to Juno MWR observations or evaluate any atmosphere profile model to determine if it results in the MWR observed
 136 brightness temperatures. We describe and test several published Jupiter atmospheric models against MWR data in
 137 Section 4. In our analysis, all of the geometries of the spacecraft and the antenna beam coverage are calculated using
 138 SPICE kernel information [Acton, 1996]. The synchrotron emission and galactic background are accounted for
 139 appropriately as described in Oyafuso et al. 2020 and Adumitroaie et al. 2016. In order to verify any proposed
 140 atmosphere model with ammonia, water and temperature profiles, we run the radiative-transfer code JAMRT
 141 [Janssen et al. 2013] to simulate the radiative-transfer process and obtain the brightness temperatures at various
 142 emission angles and latitudes at all MWR frequencies. For a standard forward model, JAMRT takes in user-
 143 specified NH_3 and H_2O enrichment, an adiabatic temperature profile is then calculated. In a simple standard model,
 144 NH_3 and H_2O abundances are uniform in the deep atmosphere and become saturated above the corresponding cloud
 145 level. However, JAMRT also allows user-specified $\text{NH}_3/\text{H}_2\text{O}$ abundances and temperature profiles. With six MWR
 146 channels sensitive to different pressure levels down to more than 250 bars, the residual values show directly if the
 147 composition distribution produced by the atmospheric model is compatible with the data. The effects of ammonia,
 148 temperature and water distributions on brightness temperature are entangled and deciding whether a specific model
 149 is the best one may not be possible using MWR data alone. However, our residual analysis process can determine
 150 whether the model is possible in the sense of being consistent with the MWR observations. We calculate the residual
 151 value of all observations, each corresponding to an observed emission angle, latitude and longitude, which indicates
 152 how well the proposed model matches the actual Jupiter observations. At any specific latitude, trends in the residual
 153 values with respect to the emission angles reveal how well the limb darkening in the proposed model matches the
 154 real case. If at large emission angles, the residual values have a downward trend, a larger limb-darkening than the
 155 proposed value is observed by the MWR observations. We will review test cases in Section 4 and explain more
 156 about how to interpret the output residual values in terms of Jupiter's atmospheric properties.

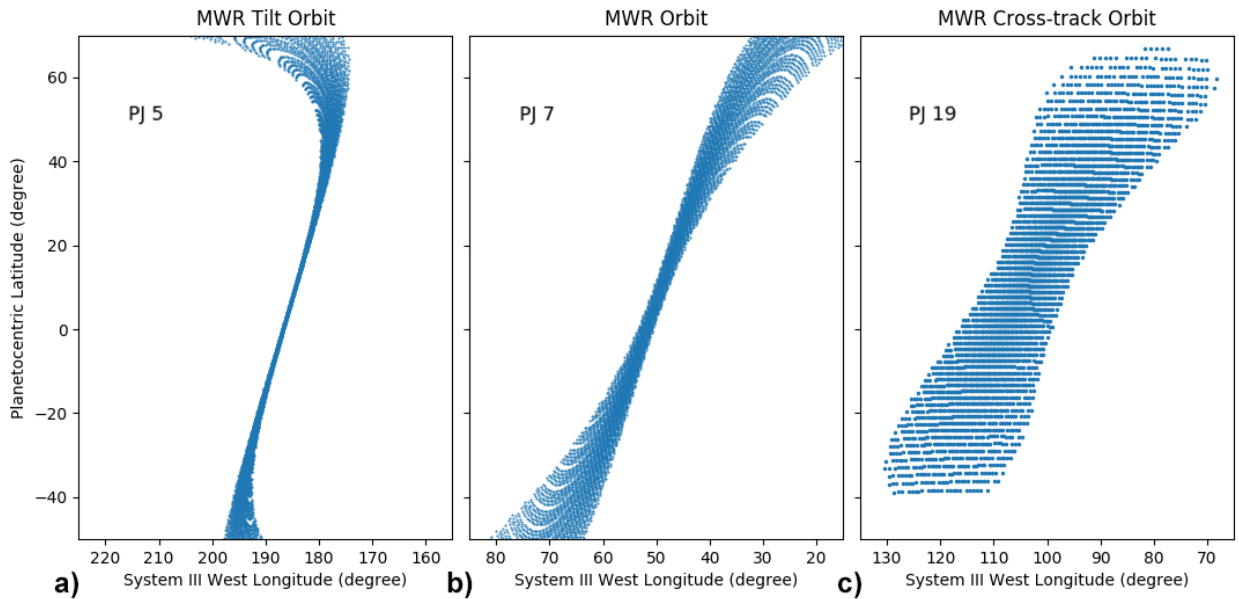
158 Based on the residual analysis described above, we also developed an iterative approach that takes any initial
 159 brightness temperature model, calculates the residual values, updates the brightness temperature model based on the
 160 residual values, and uses the updated model as a new input brightness temperature in the next iteration. The goal of
 161 this process is to converge on a best estimate of Jupiter's brightness distribution along with its emission angle
 162 dependence. We iterate the process until the residual values converge and approach zero. This iterative process is a
 163 good way to investigate small longitudinal and latitudinal structures, and make 2D brightness-temperature maps
 164 (with respect to latitude and longitude) of Jupiter at MWR observed pressure levels. At each iteration i , we begin
 165 with convolving the regularly gridded input model $Model^i(\text{emissionangle}, \text{latitude}, \text{longitude})$ with the MWR beam
 166 pattern coverage and generate simulated antenna temperatures $T_{a_model}^i(\text{Obs}_{emiss}, \text{Obs}_{lat}, \text{Obs}_{lon})$ for each observation
 167 point. The regularly gridded input model $Model^i(\text{emissionangle}, \text{latitude}, \text{longitude})$ is in units of brightness temperature
 168 at a series of emission angle grids on each Jupiter's latitude- longitude- grid. We then subtract the modeled antenna
 169 temperature from the observed antenna temperature and derive the output residual values
 170 $Residual^i(\text{Obs}_{emiss}, \text{Obs}_{lat}, \text{Obs}_{lon}) = T_{a_obs}^i(\text{Obs}_{emiss}, \text{Obs}_{lat}, \text{Obs}_{lon}) - T_{a_model}^i(\text{Obs}_{emiss}, \text{Obs}_{lat}, \text{Obs}_{lon})$, which serve as a proxy
 171 for the difference between the input brightness temperature model and the real Jupiter brightness temperature at the
 172 corresponding boresight emission angle, latitude and longitude. We introduce the parameter:

$$174 \quad T_{best}^i(\text{Obs}_{emiss}, \text{Obs}_{lat}, \text{Obs}_{lon}) = Residual^i(\text{Obs}_{emiss}, \text{Obs}_{lat}, \text{Obs}_{lon}) + T_{model}^i(\text{Obs}_{emiss}, \text{Obs}_{lat}, \text{Obs}_{lon}) \quad (4)$$

176 where $T_{model}^i(\text{Obs}_{emiss}, \text{Obs}_{lat}, \text{Obs}_{lon})$ is the brightness temperature at the observation point according to the input model,
 177 and $T_{best}^i(\text{Obs}_{emiss}, \text{Obs}_{lat}, \text{Obs}_{lon})$ is an updated and better estimation for Jupiter's brightness temperature at this specific
 178 observing geometry. Constrained by the finite size of our beam and the fact that we lack perfect knowledge of the
 179 brightness temperature distribution in adjacent positions at the beginning of this iteration process,
 180 $T_{best}^i(\text{Obs}_{emiss}, \text{Obs}_{lat}, \text{Obs}_{lon})$ will tend to approach the real Jupiter brightness temperature value after each iteration.
 181 Several iterations are expected to be needed to achieve a value within measurement uncertainty.

183 A crucial step in this iteration process is to update the Jupiter model at the end of each iteration. For typical Juno
 184 MWR orbits, each latitude was observed at multiple emission angles and within a small longitudinal range (see
 185 Figure 2, middle panel, as an example of a typical MWR observation track), which is necessary for determining the
 186 limb-darkening value and diminishing the longitudinal variation in each latitude bin. This is accomplished with the

187 spacecraft spin axis orthogonal to its orbital plane and the MWR antenna beams sweeping north to south (antennas
 188 fixed to the spacecraft) as the Juno spacecraft also passes over the planet from north to south. A second and special
 189 case is the MWR tilt orbit (Fig. 2 left panel), which is designed to minimize the longitudinal coverage (the
 190 spacecraft attitude is slightly tilted to compensate for Jupiter's rotation) and provide data for more accurate analysis
 191 of nadir brightness and limb darkening. For typical MWR orbits, we first ignore the longitudinal variation and derive
 192 the best-fit brightness model with respect to latitudes and emission angles. After that, with the knowledge of the
 193 limb-darkening values, we fix the limb darkening and further derive the best-fit nadir brightness temperature model
 194 with respect to latitudes and longitudes in order to reveal small longitudinal structures. The cross-track orbit is yet
 195 another special MWR orbit [Janssen et al. 2017] (Fig. 2 right panel), where at each latitude a wide range of
 196 longitudes are observed but each longitude was only observed once at a specific emission angle. The spacecraft spin
 197 axis is parallel with Jupiter's spin axis and the antenna beams sweep from east to west (from lower to higher west
 198 longitudes in System III), across the planet as the spacecraft spins. In these cases, at each latitude the variations due
 199 respectively to longitudinal structure and limb darkening are entangled and impossible to distinguish. Therefore, a
 200 prior value for the limb darkening at each latitude becomes important. For different data features and also for
 201 comparison purposes, we proposed four model-updating methods as described below.
 202



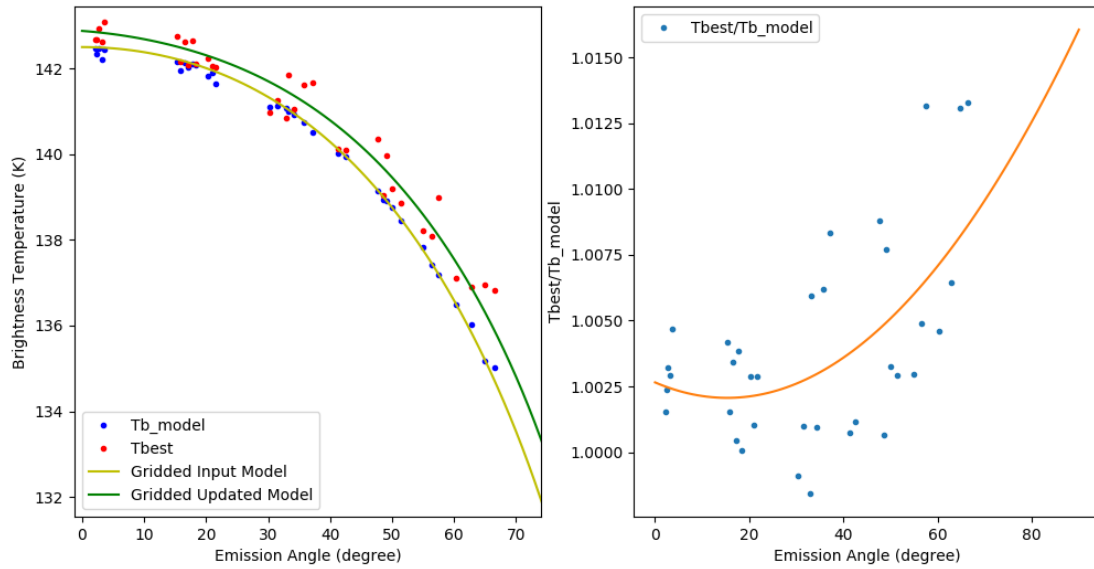
203 **Figure 2.** MWR observation tracks for an MWR tilt orbit (left panel, PJ5 as an example), a typical MWR orbit
 204 (middle panel, PJ7 as an example) and an MWR Cross-track orbit (right panel, PJ19 as an example).
 205
 206

- 207 (1) Method 1: Interpolate and smooth among T_{best}^i with respect to emission angles.
 208

209 For typical MWR orbits and MWR tilt orbits with narrow longitudinal coverage, method 1 is used to derive
 210 a brightness temperature model with respect to latitudes and emission angles. The iteration process is not
 211 sensitive to the initial model and the residuals converge to near zero usually after 5 iterations. We assume
 212 that at iteration i the input gridded model is $Model^i(emissionangle, latitude)$ covering 90° S to 90° N. In the left
 213 panel of Figure 3, blue points show the brightness temperature model $T_{model}^i(Ob_{emiss}, Ob_{lat})$ for each
 214 observation point within one latitude bin at the beginning of this iteration, which is based on the input
 215 gridded model $Model^i(emissionangle, latitude)$ (yellow curve). At the end of this iteration, we obtain updated
 216 brightness temperatures for each observation point $T_{best}^i(Ob_{emiss}, Ob_{lat}) = Residual^i(Ob_{emiss}, Ob_{lat}) + T_{model}^i(Ob_{emiss}, Ob_{lat})$ (see
 217 red points in left panel of Fig. 3). We introduce the factor $f = \frac{T_{best}^i(Ob_{emiss}, Ob_{lat})}{T_{model}^i(Ob_{emiss}, Ob_{lat})}$ (see blue points in right panel of
 218 Fig. 3). Within each latitude bin, we fit a smooth spline curve function $func(emissionangle)$ to factor f with
 219 respect to the emission angle (Fig. 3, orange curve in right panel) and update the model
 220 with $Model^{i+1}(emissionangle, latitude) = Model^i(emissionangle, latitude) * func(emissionangle)$. In the left panel of Fig. 3, the
 221 green curve shows the updated brightness model, which will be used in the next iteration. Thus, we are able

222
223

to find an updated Jupiter model that catches the main trend in T_{best}^i variation against emission angle, while minimizing the effect from longitudinal variations.

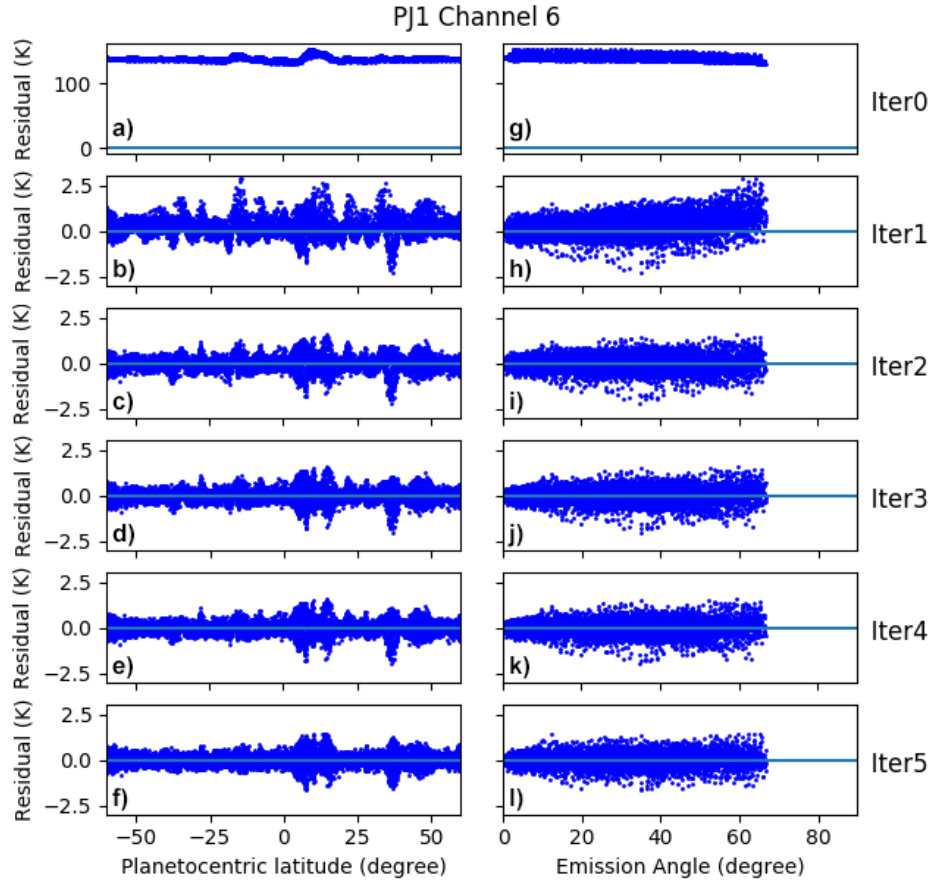


224
225
226
227
228
229
230
231

Figure 3. Example of model updating method 1 at an iteration i in one latitude bin of width 0.5° . Left panel: the yellow curve shows the input gridded model at the beginning of this iteration and the green curve is the updated model. Blue points show the brightness-temperature model for each observation and red points are the updated brightness at the end of this iteration. Right panel: the blue points show the value of factor f with respect to emission angle, which is then fit with the orange curve, a smooth spline curve function.

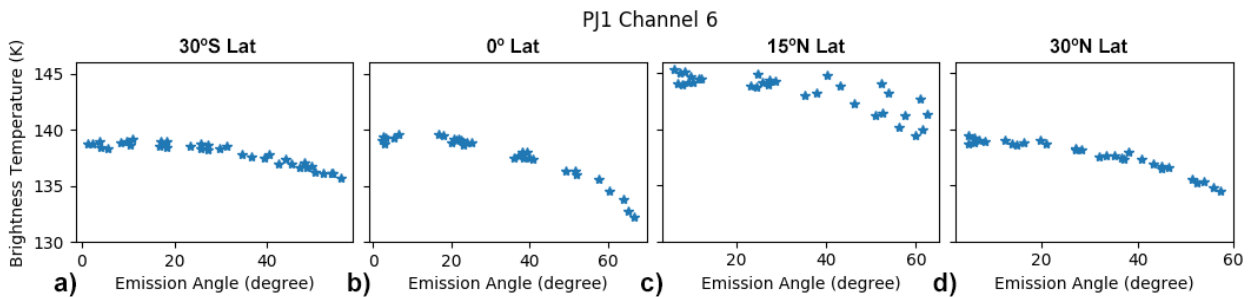
232
233
234
235
236
237
238
239
240
241
242
243
244
245
246
247
248
249
250
251
252
253

The iteration process is not sensitive to the initial guess of the brightness model. In Figure 4, we show the iterative results (residual values with respect to latitudes (left column) and emission angles (right column)) for PJ1 Channel 6 through 5 iterations as an example, starting with a globally uniform 1K brightness temperature, zero limb-darkening model, which has zero Jupiter brightness information. The right bottom panel in Fig. 4 shows the final residual values with respect to emission angle for all latitudes, which reveals how well the limb darkening value matches the real case. After 5 iterations, the tilting trend with respect to emission angle is within error bars determined by the instrument performance model. We used model updating method 1: “Interpolate and smooth among T_{best}^i with respect to emission angle” in this test case. Even starting with a model with no real Jupiter brightness temperature information, the residual values approach zero after 5 iterations and obvious structures are minimized in the final residual values with respect to latitude or emission angle. Therefore, we can conclude that the final brightness-temperature model is a good approximation to the real Jupiter brightness temperature according to MWR observations. It is consistent with observations at the $1-\sigma$ level, with all latitudes within expected error bars. Figure 5 shows the final best-fit model at four latitudes, where the initial models are 1K at all latitudes and emission angles. In Fig. 4f, we noticed that although the overall offset of the residuals is less than 2% ($\sim 3\text{K}$) and the residuals approach the $\sim 0.3\text{K}$ instrument noise at most latitudes after 5 iterations, at certain latitude bins (such as around 5°N to 20°N and around 35°N) the standard deviation is obviously larger than at other latitudes. This can also be seen in Fig. 5 where at 15°N , the brightness temperature vs. emission angle curve has more spread. This can be attributed to small longitudinal or temporal structures, which will be dealt with later using model update method 4 – “Fix limb-darkening values”.



254
255
256
257
258
259
260
261
262
263

Figure 4. Results from iterative residual analysis on PJ1 channel-6 observations. Panels a-f: residual values with respect to latitude after each iteration, which approach a mean of zero after 5 iterations. Panels g-l: the same residual values with respect to emission angle, which becomes flat after 5 iterations. From the instrument performance model [Janssen et al, 2017], the overall offset of the residuals should be less than 2%, which is $\sim 3\text{K}$. In the final iteration, the residuals approach the $\sim 0.3\text{K}$ instrument noise at most latitudes, with exceptions which we attribute to spatial variations not accounted for in this longitudinally-averaged model.



264
265
266
267
268
269
270
271

Figure 5. The best-estimated brightness temperature $T_{best}(Obs_{emiss}, Obs_{lat})$ for observations in latitude bins (a) 30°S , (b) 0° , (c) 15°N , and (d) 30°N after 5 iterations (blue markers), starting with a uniform initial model (1K at all latitudes and all emission angles).

(2) Other model updating methods for longitudinally-uniform models

272
 273
 274
 275
 276
 277
 278
 279
 280
 281
 282
 283
 284
 285
 286
 287
 288
 289
 290
 291
 292
 293
 294
 295
 296
 297
 298
 299
 300
 301
 302
 303

For comparison purposes, we introduced two additional model updating methods to derive brightness models with respect to latitudes and emission angles.

(2.1) Method 2: Fit to 3 coefficients

According to theoretical and empirical deduction, the Jupiter limb darkening can be approximated with the 3-coefficient equation [Oyafuso et al. 2020]:

$$T_B(\theta) = [A_0 + A_1(1 - \mu) + A_2(1 - \mu)^2] \cdot f(\theta) \quad (5)$$

where θ is the emission angle and $\mu = \cos(\theta)$. A_0 is the nadir brightness temperature, and A_1 and A_2 are the limb-darkening coefficients. $f(\theta)$ is an empirical angular profile suggested by Oyafuso et al. (2020) in order to account for the rapid brightness drop-off at larger emission angles [Figure.2 in Oyafuso et al. 2020]. At the end of each iteration and within each latitude bin, this method fits T_{best}^i with respect to μ for all the observations in that latitude bin to the equation above.

(2.2) Method 3: Spline interpolation

With this method, T_{best}^i is fitted with respect to emission angle with a spline function. Though MWR also observes Jupiter at high emission angles, due to the large main-beam coverage as projected onto the planet at high emission angles and significant synchrotron leakage into the beam in Channels 1 and 2, we only use observations with emission angles less than 60° ($\mu > 0.5$) to update the Jupiter model. The spline-interpolation method is able to match the brightness temperature variations at these small to medium emission angles, but fails to imitate the rapid drop off at emission angles close to 90° .

In Figure 6, we show examples for updating a brightness-temperature model at Channel 6 from iteration 1 to 2 (with respect to emission angle) at two latitude bins, 70°S and 0° , respectively, using the three different methods described above. The spline-fit results are not able to match the rapid drop of brightness temperature around 90° emission angle, while the 3-coefficient fit drops fastest there due to the imposed empirical angular profile.

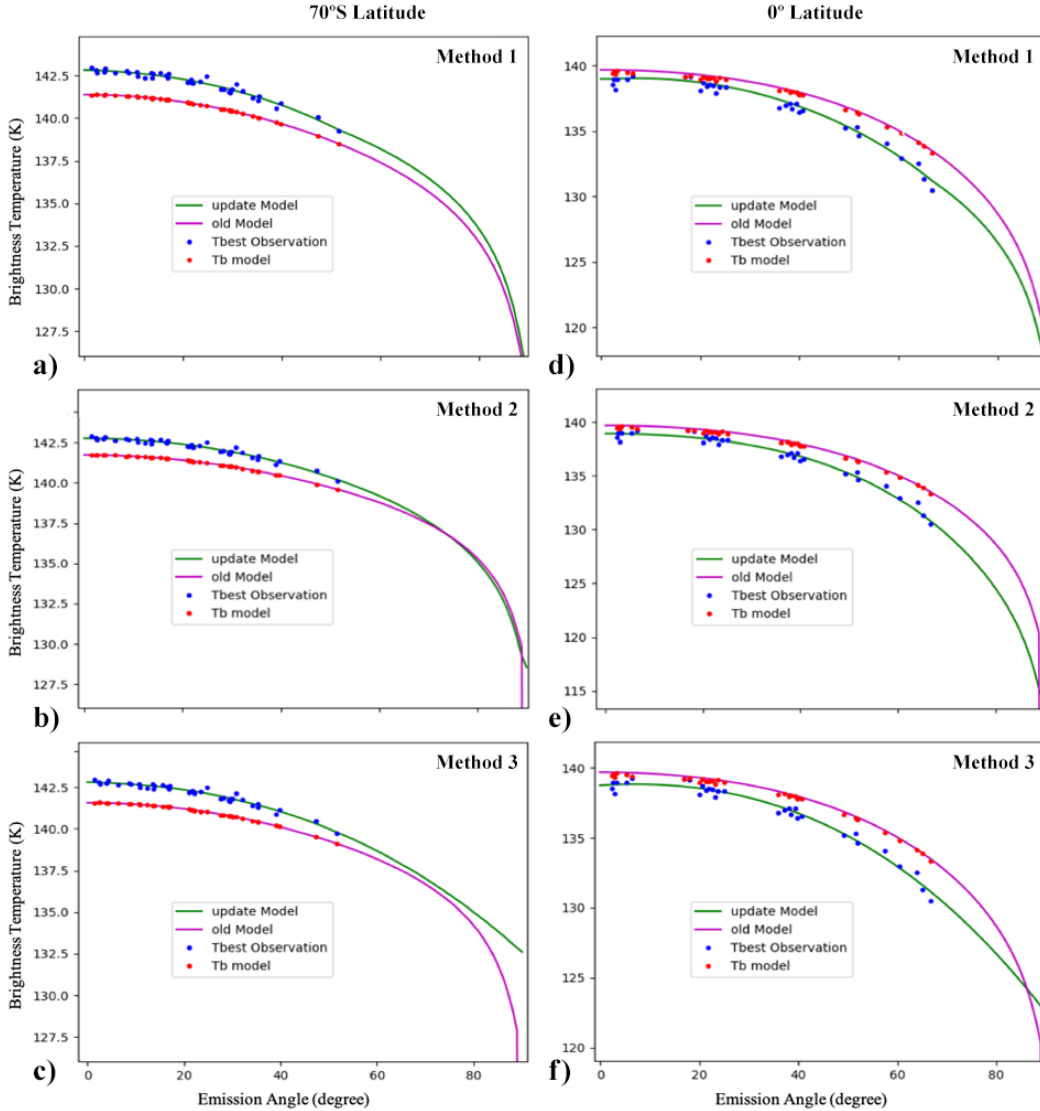


Figure 6. Comparison between three model-updating methods when deriving a brightness-temperature model with respect to latitude and emission angle (Channel 6 data as an example). In each panel, red dots show the T_{model}^1 derived from input regularly gridded model (magenta curve) at the beginning of iteration 1 and blue dots show the T_{best}^1 which is then used to derive the updated model (green curve) for the next iteration.

(3) Method 4: Fix limb darkening.

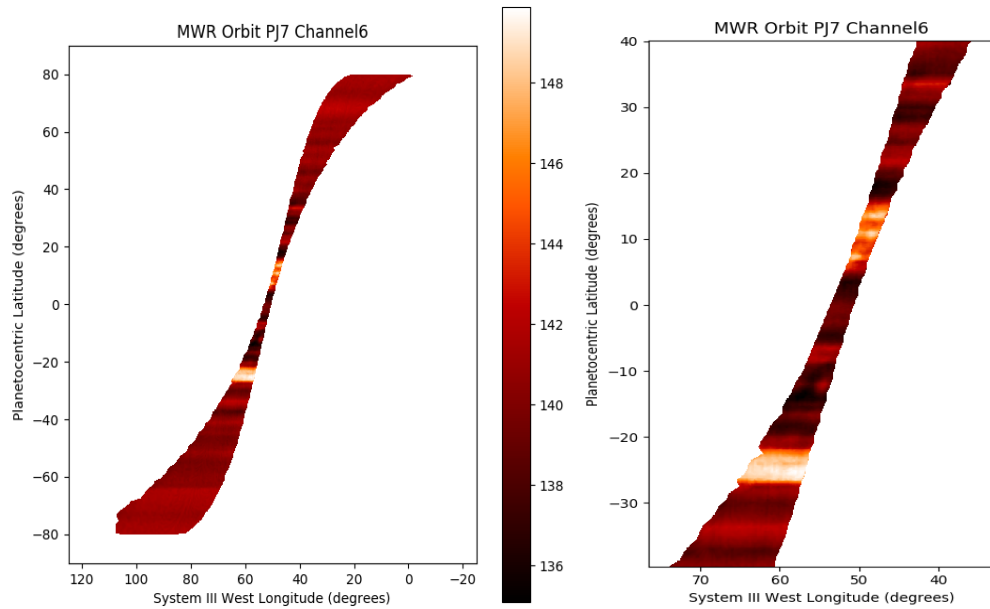
As described earlier in Section 3, for typical Juno MWR orbits, each latitude was observed at multiple emission angles and within a small longitudinal range. In these cases, we iterate the process with model-update method 1 to achieve a longitudinal average (considering that the longitudinal range is rather narrow) while varying the limb darkening profile at all latitudes for each perijove, and then apply the limb-darkening profile and iterate with model-update method 4 to obtain the longitudinal variation in nadir brightness temperature. We fix the limb-darkening values, and only nadir brightness temperature at various latitudes and longitudes are updated during these iterations. At the end of each iteration i , T_{best}^i is corrected to the nadir direction by:

323
324
325
326
327
328
329
330
331
332
333
334
335

$$T_{best_nadir}^i(0, Obs_{lat}, Obs_{lon}) = T_{best}^i(Obs_{emiss}, Obs_{lat}, Obs_{lon}) * \frac{T_{model}^i(0, Obs_{lat}, Obs_{lon})}{T_{model}^i(Obs_{emiss}, Obs_{lat}, Obs_{lon})} \quad (6)$$

$T_{best_nadir}^i(0, Obs_{lat}, Obs_{lon})$ is then used to update the Jupiter nadir brightness-temperature model on a regular grid. One specific use of this method is to study longitudinal structures and make 2D (latitude, longitude) Jupiter nadir brightness-temperature maps (see Figure 7 as an example for PJ7 Channel 6), which can be compared with visible upper atmosphere features in order to reveal deep structures connected to those features.

As for the special Juno cross-track orbits (such as PJ19), these perijove observations alone are not able to determine longitudinal structures and limb darkening values at the same time. Therefore, we take averaged limb-darkening values from previous perijoves (PJ1 to PJ9) as prior and iterate with model-updating method 4 to make 2D (latitude, longitude) maps [Bolton et al. 2020].



336
337
338
339
340
341
342
343
344
345
346
347
348
349
350
351
352
353
354
355
356
357

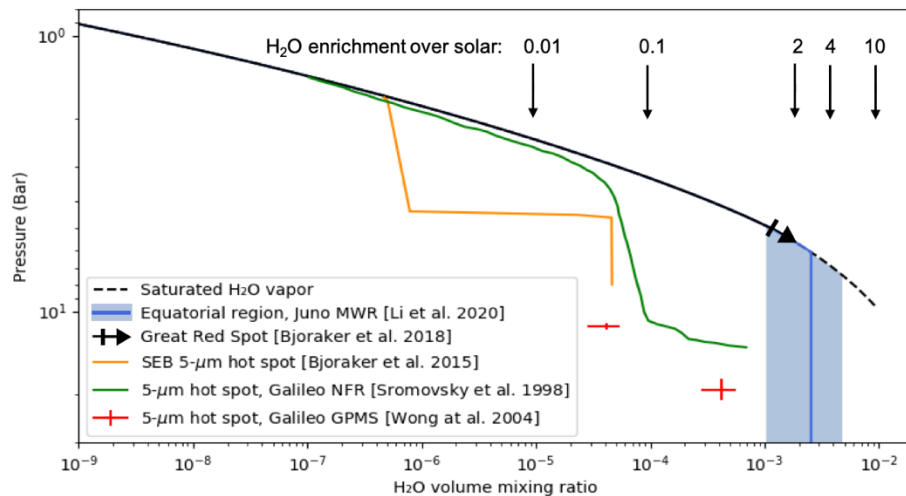
Figure 7. 2D (latitude, longitude) nadir brightness temperature map for PJ7 Channel 6 obtained after the iterative process with model updating method 4, which reveals small longitudinal structures, with a blow up map in latitude range 40° S to 40° N on the right.

4. Test Cases - Test Jupiter atmosphere models against MWR observations

To examine our residual-analysis process and to investigate the science results from it, we test a few previously published ammonia and water concentration profiles against the MWR observations. At microwave frequencies, ammonia, as the main opacity source, affects the brightness temperature most significantly, while on the other hand the water abundance would affect the atmospheric structure through latent heating and molecular weight effects. The behavior of residuals with respect to latitude and emission angle indicates how well a given profile matches the real Jupiter atmosphere and what modification should be made to better match the observations. Note that the variation in the MWR data due to the instrument noise should be quite small, but none of the models shown here attempt to take into account longitudinal or temporal variations. It is therefore not surprising that the residuals in the following test cases show more variation than instrument noise alone.

The bulk oxygen elemental ratio in Jupiter determines the water abundance in its atmosphere assuming a compositionally homogeneous envelope, and is key to discriminating among models for the origin of Jupiter and accretion processes in the planet-forming disk. The water abundance prior to Juno was measured by the Galileo Probe Mass Spectrometer (GPMS) as subsolar down to at least 19 bars [Wong et al. 2004]. Wong et al. 2004 reported a mole fraction of H₂O of $(4.1 \pm 1.3) \times 10^{-5}$ at 11.0-11.7 bars and $(4.2 \pm 1.4) \times 10^{-4}$ at 17.6-20.9 bars,

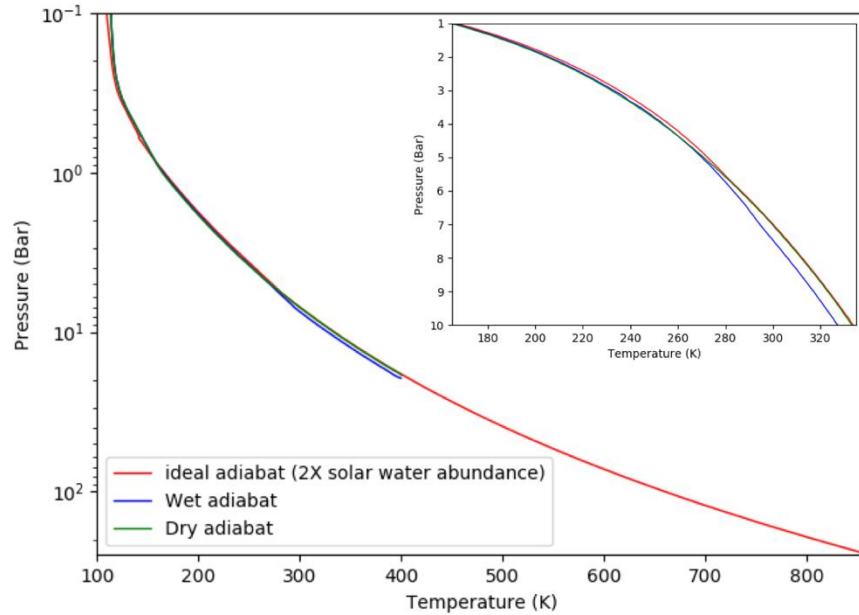
358 which are both averages of data spanning the corresponding pressure range. However, the mixing ratio of H₂O in the
 359 deep well-mixed atmosphere was not measured with GMPS and may be higher at deeper levels. Niemann et al. 1998
 360 reported an upper limit to H₂O of 8×10^{-7} at 2.7 bar. More recently, ground-based infrared spectroscopy has
 361 constrained water abundance profiles in Great Red Spot (GRS) spectra as well as typical belt and zone spectra
 362 [Bjoraker et al. 2015, 2018]. The GRS spectrum requires a water cloud top at $p \geq 5$ bar, inducing a O/H lower limit
 363 of $1.1 \times$ solar (corrected to the protosolar O/H ratio of Asplund et al. 2009) [Bjoraker et al. 2018]. They also found
 364 that the South Equatorial Belt (SEB) hot spot follows the H₂O profile observed by the Galileo Probe Mass
 365 spectrometer (GMPS) and becomes very dry above at $P < 4.5$ bars. The South Tropical Zone (STZ) has a saturated
 366 H₂O profile until reaches its cloud top between 4 and 5 bars [Bjoraker et al. 2018]. On the other hand, the water
 367 vapor profile retrieved from the Galileo probe Net-Flux Radiometer (NFR) measurements [Sromovsky et al. 1998]
 368 shows significantly sub-saturated water abundance at pressures greater than approximately 1.5 bars. Li et al. 2020
 369 reported on the water abundance in the equatorial region, defined as from 0 to 4° north latitude, to be $2.5^{+2.2}_{-1.5} \times 10^3$
 370 ppm, or $2.7^{+2.4}_{-1.6}$ times the protosolar oxygen elemental ratio to H, based on 1.25 to 22 GHz (1.4 to 24 cm) data from
 371 Juno MWR probing approximately 0.7 to 30 bars pressure. In Figure 8 we show various profiles of H₂O derived
 372 from ground-based, Galileo Probe, and Juno data. Arrows denote the water volume mixing ratio corresponding to
 373 O/H enrichments ranging from 0.01 to 10 times solar. Ground-based retrievals are shown for a 5- μ m Hot Spot in the
 374 South Equatorial Belt and for the Great Red Spot, which follows a saturated profile above an opaque cloud at 5 bars.
 375 Water abundances derived from two investigations on the Galileo Probe are also shown. The continuous profile is
 376 from the Net Flux Radiometer; the points with error bars are from the Galileo Probe Mass Spectrometer. Finally, the
 377 recent H₂O measurement in the Equatorial Zone by Li et al. (2020) from Juno/MWR is shown in blue along with its
 378 error bars in light blue shadowed area. The difference between the derived H₂O abundances from Juno/MWR and
 379 Galileo is likely because the 5- μ m Hot Spot Galileo probe entered was particularly dry, whereas the MWR
 380 measured H₂O in the Equatorial Zone.



381
 382 **Figure 8.** Water abundance distribution profiles in and below the cloud condensation region for different assumed
 383 bulk abundances [Sromovsky et al. 1998, Bjoraker et al. 2015, Wong et al. 2004]. Blue line with shadowed area
 384 shows $2.7^{+2.4}_{-1.6}$ times the protosolar oxygen elemental ratio to H at 0° to 4° North [Li et al. 2020]. The black arrow
 385 shows the opaque water cloud at $p \geq 5$ bar at Great Red Spot (GRS), with a saturated H₂O profile above [Bjoraker
 386 et al. 2018]. The solar photospheric abundance is according to Asplund et al. 2009, adjusted to protosolar values.

387
 388
 389 Based on Juno/MWR PJ1 nadir brightness-temperature data, Li et al. (2017) (hereafter, Li17) published an ammonia
 390 concentration profile for pressures from 0.5 bar to approximately 200 bars, with a deep ammonia abundance of
 391 $\sim 3.5 \times 10^{-4}$. Their profile shows a depletion of ammonia over the specified latitude range down to a hundred bars
 392 and a column of high-concentration ammonia gas in the northern equatorial zone (EZ). We apply their ammonia
 393 profile in the latitudinal range from 50°S to 50°N in our residual analysis. As their ammonia profiles are presented in
 394 latitude bins of about 2°, a linear interpolation is used for intermediate latitudes. The ideal adiabatic temperature

395 profile (see Figure 9) used by Li17 was derived at Equatorial Zone and then applied to all other latitudes [Li et al.
 396 2017]. The temperature profile depends on their retrieved deep ammonia and water abundance, with modification in
 397 the upper troposphere that are constrained by mid-infrared observations [Fletcher et. al 2009]. The resulting residual
 398 plots are shown in Figure 10 for MWR observations from PJ1 to PJ9 and channels 1 through 6. The panels on the
 399 left show the residuals for their model in the latitudinal direction. Their model is a local model without large-scale
 400 circulation. In channels 4, 5 and 6, although there are still latitudinal structures in the residuals for individual
 401 perijoves, when combining all the perijoves together, the mean residual values are near zero (excluding PJ7
 402 observations near the Great Red Spot). The variation across perijoves in channels 4, 5, 6 suggest unmodeled
 403 temporal or longitudinal structures. In channel 1 through 3 we see deviations around 10°N to 20°N, which shows up
 404 in all perijoves, suggesting that a different ammonia volume mixing ratio or temperature profile is needed at 10 bar
 405 and deeper at those latitudes.
 406

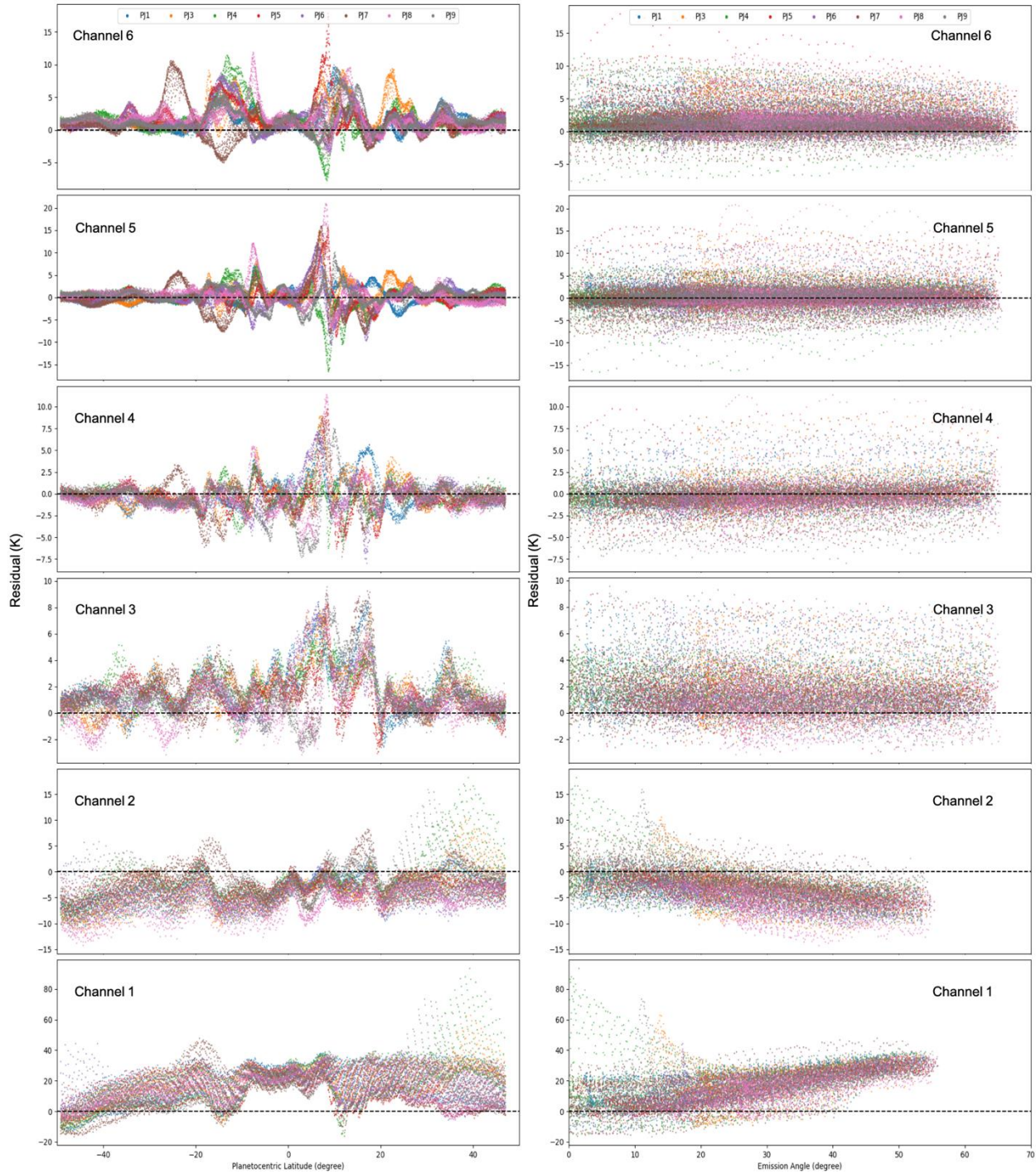


407
 408
 409 **Figure 9.** Temperature profiles used in the test cases. Red: Ideal adiabatic temperature profile assuming 2 solar
 410 water abundance in the deep atmosphere. Blue and green: wet and dry adiabatic temperature profile proposed by de
 411 Pater et al. 2019. The inserted figure shows a blow-up of these temperature pressure profiles at 1-10 bars in linear
 412 scale of pressure.
 413

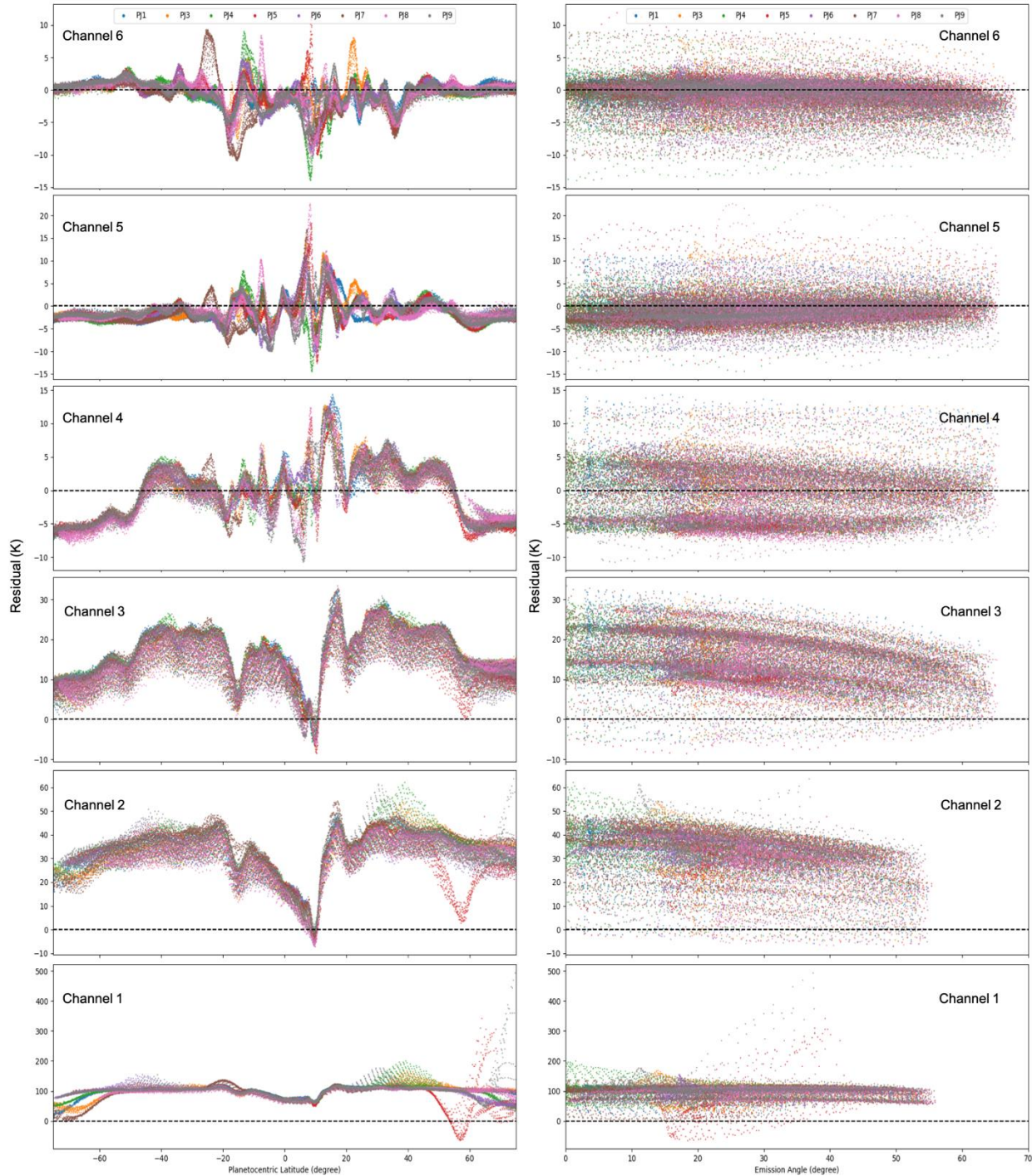
414 With the limited knowledge of synchrotron radiation and ammonia/water opacities in the deep atmosphere observed
 415 by channel 1, matching the observations becomes especially difficult. On the other hand, a deviation of temperature
 416 from ideal adiabat that Li17 assumed is also a possibility. The panels on the right in Fig. 10 show how the residuals
 417 distribute with respect to emission angles, which is a very important indication for whether the input atmosphere
 418 profile generates the correct limb darkening. In Channels 3 to 6, all the distributions are rather flat and thus we see
 419 no systematic problem with the limb darkening. But in Channel 1 and 2, residuals deviate further from 0 at larger
 420 emission angles. There is potential confusion between effects from errors in the temperature profile or from greater
 421 synchrotron contribution to the antenna temperature at larger emission angles. However, differences in spacecraft
 422 pointing from orbit to orbit would lead to systematic, orbit-dependent trends in the high-emission angle residuals if
 423 synchrotron emission were the dominant source of error. Instead, the residuals point to errors at high emission angle
 424 that are consistent from orbit to orbit. Due to the high residuals at large emission angles, for channel 1 and 2, Li17
 425 focused on data with emission angles smaller than 40°. A more detailed reexamination of the assumptions they made
 426 in their model would be helpful in better understanding the MWR data.
 427

428 Soon after Li17, de Pater et al. 2019 analyzed VLA observations (hereafter, dePater19) between 3 to 37 GHz. Their
 429 longitude-smear spectra show high NH₃ abundance of vmr 4.1×10^{-4} in the deep atmosphere ($P > 8 -$
 430 10bars), decreasing at higher altitudes (see black line in Figure 13 for their profile at 6.5°N). As shown in Fig. 13,
 431 the deep ammonia abundance derived by dePater19 and Li17 are rather close, however, dePater19 shows ammonia

432 depletion only to 8-10 bars (at most 20 bars at NEB), while Li17 showed such depletion much deeper, persisting
433 down to 50-60 bars. The VLA observations were not able to see the atmosphere deeper than 10 - 20 bars because of
434 strong synchrotron radiation in the foreground at longer wavelength. Both works show a high ammonia
435 concentration in the northern Equatorial Zone ($\sim 0^\circ - 5^\circ$ N). Another big difference is that Li17's results show a
436 unique ammonia concentration with slight increase with altitudes starting from about 7 bars to 2 bars and a relatively
437 high abundance just below the NH_3 cloud layer, while the dePater19's ammonia concentration profile monotonically
438 decreases with altitude, from well-mixed in the deep atmosphere to the ammonia cloud bottom. This pressure range
439 is most sensitive in Juno/MWR Channels 3 through 6. To calculate the residuals of the dePater19 profile in the
440 latitude range from 75° S to 75° N, we employed their dry and wet adiabatic temperature profiles (Fig. 9) and 4
441 times solar water abundance in the deep atmosphere as they proposed [de Pater et al. 2019]. As we compared the
442 residual results from the dePater19 model (Figure 11) with the residual results from Li17 (Fig. 10), in channel 5 and
443 6, which is sensitive to $P < 4$ bars and most sensitive around 1 -2 bars for channel 5, 0.5 - 0.6 bars for channel 6,
444 both dePater19 and Li17 fit the MWR observations from PJ1 to PJ9 comparatively well at low latitudes. However,
445 in channel 5 dePater19 starts to deviate from MWR data from mid- to high- latitudes. In Figure 12, we show the
446 mean and standard deviation of residuals in 2° latitude bins (left column) and 2° emission angle bins (right column)
447 from both Li17 (orange curve) and dePater19 (blue curve). The values are derived from residuals in Fig.10 for Li17
448 and in Fig.11 for dePater19 combining all PJ1 to PJ9 results. In Channel 6, at low- to mid- latitudes, both Li17 and
449 dePater19 have mean residuals close to zero while both miss some small latitudinal structures. In Channel 5, both
450 models match the observations at low latitudes, while dePater19 misses more small latitudinal structures. At mid-
451 high- latitudes, Li17 matches the observations better than dePater19 in channel 5. The mean residuals with respect to
452 emission angles are flatter for the Li17 model, with an offset less than 1K for channel 6 and 5 within the 2%
453 absolute calibration uncertainty. However, there is a downward tilt at large emission angle for dePater19 in Channel
454 6, suggesting a larger limb darkening is required by the observations. In Channel 4, which is sensitive to $P < 10$ bars
455 and especially around 3 - 5 bars, both dePater19 and Li17 models match the observations from 20S to 10N.
456 However, outside this latitude, residuals from dePater19 start to deviate from zero. dePater19 residuals are
457 significantly off-zero in Channel 3, which is sensitive to $P < 40$ bars and most sensitive around 8 - 10 bars. For
458 channel 1 to 3, the residual vs emission angle panel for dePater19 is tilted downwards at larger emission angles,
459 suggesting the limb darkening in dePater19 is rather small compared to the real Jupiter atmosphere. At the same
460 time, Li17 residuals in channel 3 still remain around 0 and the limb darkening also matches the data well. As we go
461 deeper into the atmosphere with Channels 1 and 2, Li17 residuals are significantly closer to zero as compared to the
462 dePater19 residuals. In Channels 1, 2 and 3, dePater19 residuals are far above 0, which indicates that the MWR
463 observed brightness temperature is much higher than predicted by their model and could be a sign of too much
464 ammonia concentration in their model at $P > 10$ bars, where VLA (dePater19) were not able to observe.
465

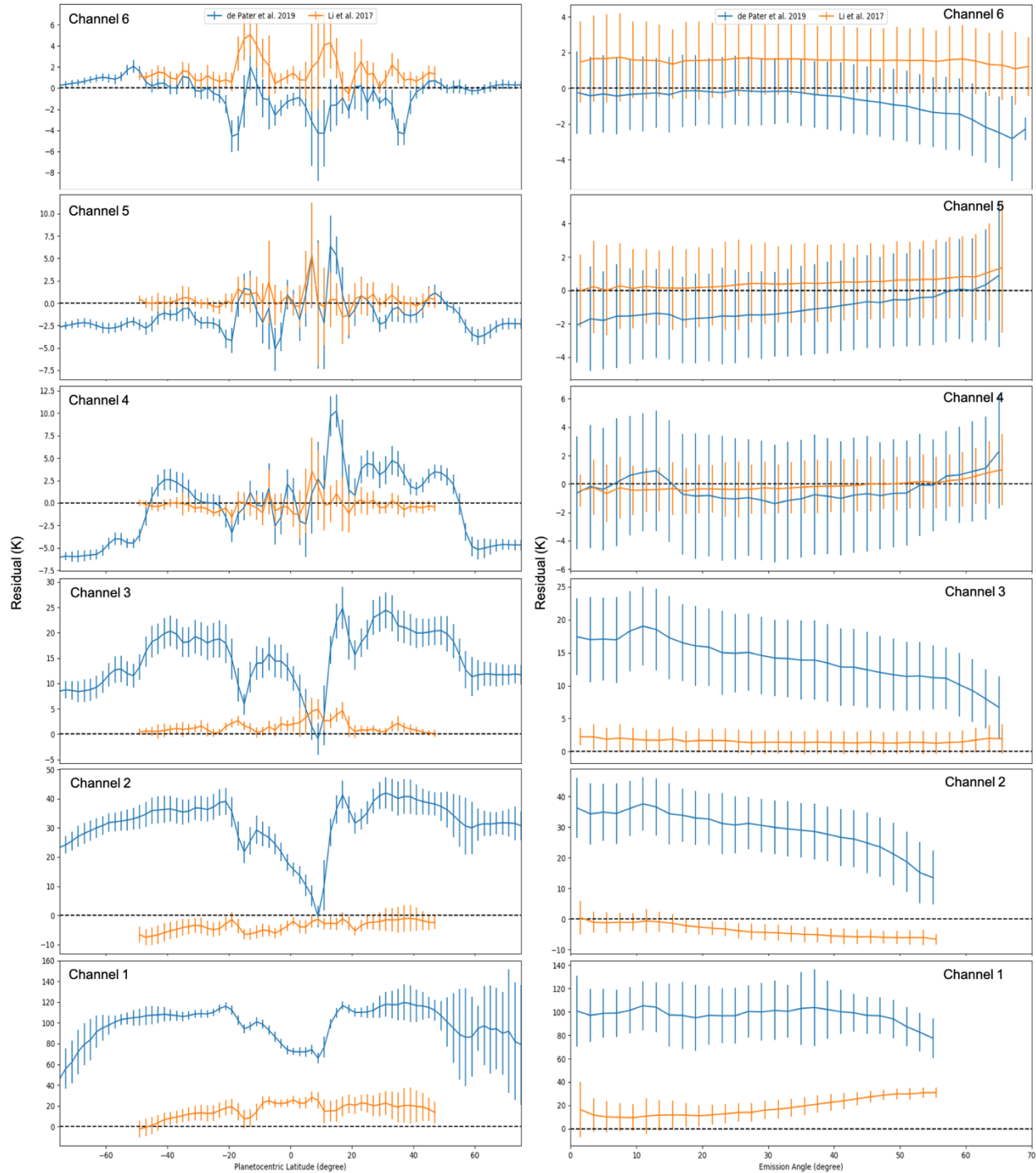


466
 467 **Figure 10.** Results for residual analysis on ammonia distribution from Li et al. 2017 using PJ1 to PJ9 observations
 468 from channel 1 to channel 6. Each perijove is plotted with different colors; blue: PJ1; orange: PJ3; green: PJ4; red:
 469 PJ5; purple: PJ6; brown: PJ7; pink: PJ8; grey: PJ9. The panels on left show the residuals of their model in the
 470 latitudinal direction; the panels on the right show how the residuals distribute with respect to emission angle.
 471



472
473
474
475
476
477

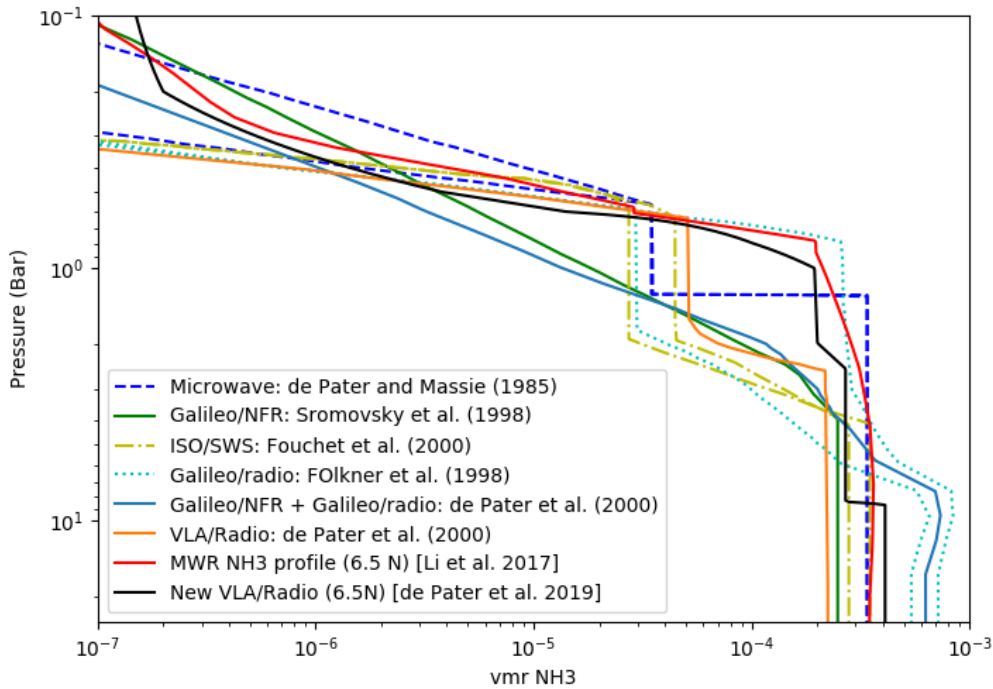
Figure 11. Results for residual analysis on ammonia distribution from de Pater et al. 2019 using PJ1 to PJ9 observations from channel 1 to channel 6. The same color code is used as given in the caption for Fig. 10. The panels on left show the residuals their model in the latitudinal direction; the panels on the right show how the residuals distribute with respect to emission angle.



478
 479 **Figure 12.** Comparison of mean and standard deviation values of residuals in 2° latitude bins (left column) and 2°
 480 emission angle bins (right column) between ammonia distributions from Li. et al. 2017 (orange) and de Pater et al.
 481 2019 (blue). The mean latitudes and emission angles in each latitude bin have been shifted 0.5° between the two
 482 models in the plot for clearer view.
 483

484 Before the arrival of the Juno spacecraft at Jupiter, Galileo Probe, which entered at a latitude of 6.5°N (the southern
 485 edge of NEB), provided the only knowledge of Jupiter’s deep atmosphere profile (i.e. temperature, water and
 486 ammonia abundances below the water cloud base). The Galileo Probe Mass Spectrometer (GPMS) estimated an
 487 NH_3 VMR of $5.7 \pm 2.2 \times 10^{-4}$ in the 8.9–11.7 bar region [Wong et al. 2004], and Galileo probe-to-orbiter signal
 488 attenuation [Folkner et al. 1998] interpreted with updated ammonia opacities [Hanley et al. 2009] found a maximum

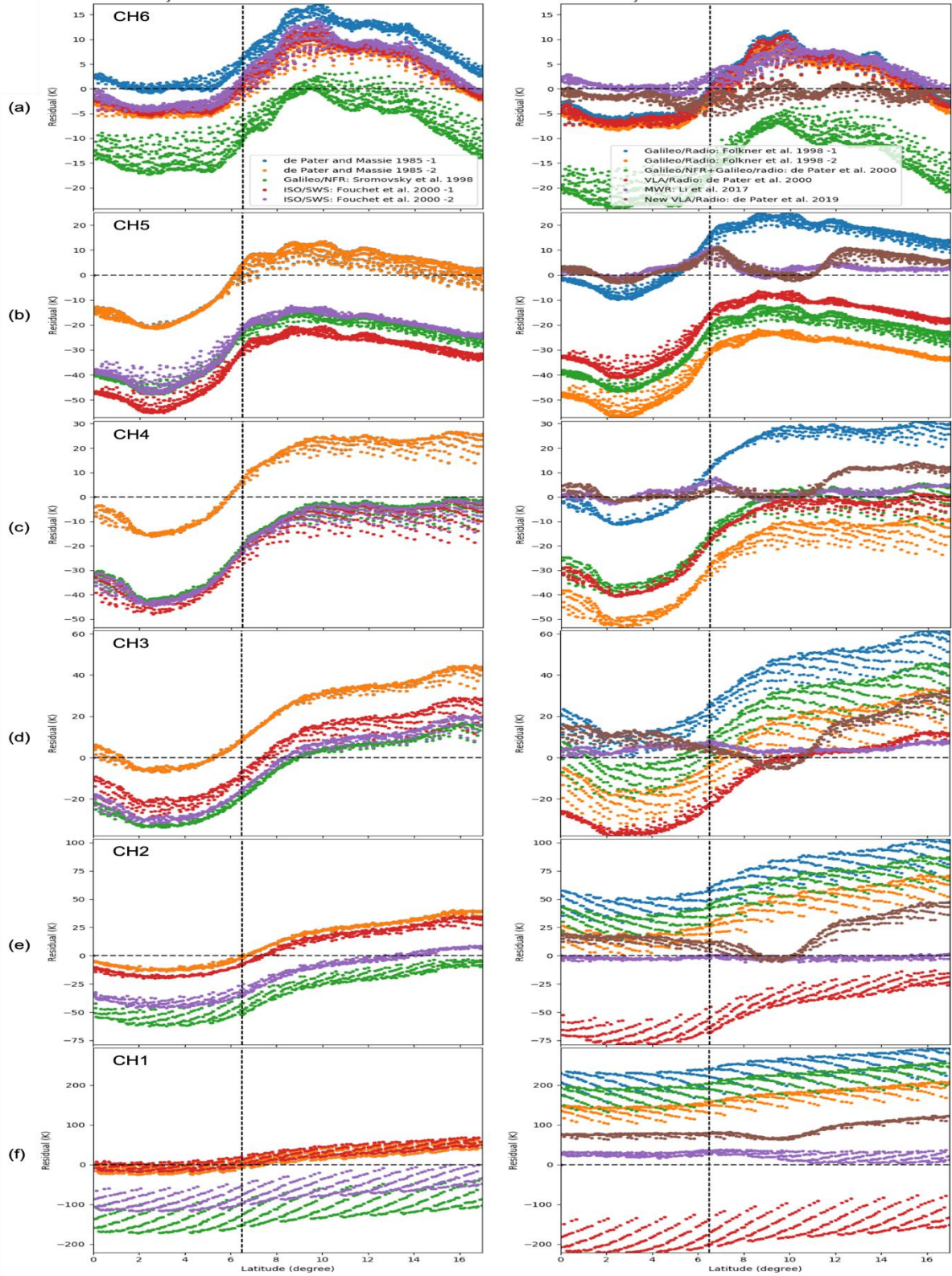
489 NH_3 VMR of $8.4 \pm 0.6 \times 10^{-4}$ at 9.7 bar (with lower NH_3 VMR at both higher and lower pressures along the probe
 490 entry path). The net flux radiometer (NFR) inferred a NH_3 VMR of 2.5×10^{-4} at $P \geq 5$ bars, dropping to about
 491 1.5×10^{-4} at 2.5 bars and then decreasing more rapidly with altitudes [Sromovsky et al., 1998]. de Pater et al. 2001
 492 presented disk-averaged brightness temperature from Very Large Array (VLA) observations showing ammonia
 493 decreasing at pressure $P \lesssim 4$ bar and a global depletion of ammonia in the region around 2 bars, reaching subsolar
 494 (≈ 0.5). All derived ammonia VMR profiles from all of these works are summarized in Fig. 13, together with the
 495 ammonia concentration profiles of Li17 and dePater19 at 6.5°N for comparison. Except for Li17 that provides
 496 ammonia distribution down to thousands of bars, all other ammonia profiles are considered reaching uniform deep
 497 ammonia abundance below ~ 20 bars. There are a few cases where two lines have the same color and style,
 498 indicating estimates of the upper- and lower- limits: the two blue dashed lines indicate the analysis of microwave
 499 data by de Pater and Massie (1985), which show NH_4SH and NH_3 cloud formation at about 1.4 and 0.5 bars with
 500 two UV photolysis effect limits in the stratosphere; the yellow dot-dashed lines represent the NH_3 profile inside
 501 (lower mixing ratio) and outside (higher mixing ratio) a hot spot from Fouchet et al. 2000 ISO-SWS observations;
 502 the cyan dotted lines show the low- and high- limits from the Galileo probe radio due to the uncertainty in their
 503 observations [Folkner et al., 1998]. In these test cases, we treat as if these ammonia abundances are globally
 504 representative, which is only true in the disk-averaged VLA results [de Pater and Massie, 1985].



505
 506
 507 **Figure 13.** Ammonia abundance distribution profiles from all previous observations around 6.5°N . Except for Li17,
 508 all other ammonia profiles are considered reaching uniform deep ammonia abundance below ~ 20 bars.
 509

510
 511 We found that the deep ammonia abundance in Li17 is very close to the ISO/SWS value outside the hot spot and the
 512 disk-averaged VLA results from de Pater and Massie (1985). When calculating the residuals for these profiles, we
 513 used the ideal adiabatic temperature profile derived by Li17 at Equatorial Zone. For each ammonia profile, we tested
 514 a range of possible water-concentration profiles as shown in Fig. 8. We show here only the results for a deep water
 515 abundance of 2 times solar value. Results for the other water profiles look similar. All of the residuals are plotted in
 516 Figure 14 (a) to (f) using MWR PJ1 data. Since only the region around 6.5°N is valid for most of these profiles, we
 517 have limited the range of latitudes from 0°N to 17°N . For comparison, we also plot the residuals for Li17 and
 518 dePater19. As we focus at 6.5°N , in the deep atmosphere (Channels 1 and 2), the de Pater and Massie 1985,
 519 ISO/SWS and Li17 models fit the MWR antenna temperature best, due to their fairly close deep ammonia

520 abundances. The spread of residuals at one latitude for certain models indicates a limb-darkening mismatch. In
521 Channels 3, 4, and 5, the disk-averaged VLA results (de Pater and Massie, 1985), Li17 and dePater19 models all
522 result in the smallest residuals at 6.5°N. ISO/SWS residuals start to deviate far from zero at channel 4 due to their
523 ammonia condensation at relatively high pressures in their abundance profile. In channel 6, at the troposphere, all
524 models coincide with the MWR observation fairly well except the Galileo Probe NFR result and the disk-averaged
525 VLA [de Pater and Massie, 1985] result with the upper-limit estimate of the effect of UV photolysis on the profile in
526 the stratosphere. Despite the difference in the ammonia profile between disk-averaged VLA (de Pater and Massie,
527 1985) result with the lower-limit estimate and Li17, they are both consistent with the MWR observations at 6.5°N
528 for channels 1 - 6. However, due to the finite size of the MWR main beam, a good-fit at one single latitude doesn't
529 guarantee that the model is close to the real Jupiter atmosphere. Even when the MWR beam is centered at 6.5° N,
530 some of the received emission originates at other latitudes.
531
532



533
534
535
536
537

Figure 14. Results for residual analysis on previous published ammonia distributions as listed in Fig.13 using PJ1 observations around 6.5°N from channel 6 (a) to channel 1 (f). For each channel, residuals from all 11 models are plotted in two panels for easier viewing.

538
539
540
541
542
543
544
545
546
547
548
549
550
551
552
553
554
555
556
557
558
559
560
561
562
563
564
565
566
567
568
569
570
571
572
573
574
575
576
577
578
579
580
581
582
583
584
585
586
587
588
589
590

5. Conclusions

We provide a direct method to compare any Jupiter atmosphere model against the MWR observations through residual analysis. By investigating the residual values at various latitudes, emission angles and channels (sensitive to conditions at pressures between ~1 and 100 bars), we are able to tell which part of the Jupiter model deviates from the observations and often what kind of modification is required. This technique may not provide a unique solution, but is useful to identify flaws in existing models. For the two latitudinally resolved models we investigated (Li17 and dePater19), they are mostly consistent with MWR observations at low- to mid- latitudes from Channel 4 to 6, with overall mean residual less or close to the absolute calibration error ~2%. However, our residual analysis from Channel 1 to 3, where ground-based VLA was not able to observe, favors Li17's ammonia profile with ammonia depletion persisting deeper down to 50-60 bars and with a slightly smaller deep ammonia abundance, while dePater19 overall mean residuals start to be over 4% and reach as high as 12% in Channel 1. Additionally, the iterative process is able to generate Jupiter brightness temperatures with respect to emission angles, latitudes and longitudes that best match the MWR observed antenna temperatures. The 2D Jupiter maps with respect to latitude and longitude at all MWR observed pressure levels are of particular interest, as they will be very useful when comparing with upper-atmosphere observations at UV, near-IR and mid-IR in order to reveal the deep structures of upper atmosphere features [Fletcher et al. 2020].

6. Acknowledgments

This work is supported by Juno mission under 699048X. The Juno MWR observations used in this analysis work are available through the Planetary Data System Atmospheres Node. Data are stored in ASCII tables with supporting documentation at:

https://pds-atmospheres.nmsu.edu/data_and_services/atmospheres_data/JUNO/microwave.html

Data files can be found at:

https://pds-atmospheres.nmsu.edu/PDS/data/jnomwr_1100/data_calibrated/.

All datasets for this research are available in the citation reference: Zhang, Zhimeng, Adumitroaie, Virgil, Allison, Michael, Arballo, John, Atreya, Sushil, Bjoraker, Gordon, ... Wong, Michael. (2020). Dataset for Residual Study: Testing Jupiter Atmosphere Models Against Juno MWR Observations [Data set]. Zenodo. <http://doi.org/10.5281/zenodo.3936065>

7. References

Acton, C.H. Ancillary Data Services of NASA's Navigation and Ancillary Information Facility. Planetary and Space Science, Vol. 44, No. 1, pp. 65-70, 1996.

Asplund, M., Grevesse, N., Sauval, A.J., Scott, P. The chemical composition of the sun. Annual review of astronomy and astrophysics, DOI: 10.1146/annurev.astro.46.060407.145222. (2009)

Atreya, S. K., P. R. Mahaffy, H. B. Niemann, M. H. Wong, and T. C. Owen, Composition and origin of the atmosphere of Jupiter-an update, and implications for the extrasolar giant planets, Planet. Space Sci. 51, 105–112, 2003.

Bjoraker, G. L., M. H. Wong, I. de Pater, T. Hewagama, M. Ádámkóvics, and G. S. Orton (2018) The Gas Composition and Deep Cloud Structure of Jupiter's Great Red Spot. The Astronomical Journal 156, 101 (15 pp.). (<https://ui.adsabs.harvard.edu/abs/2018AJ....156..101B>)

Bjoraker, G. L., M. H. Wong, I. de Pater, and M. Ádámkóvics (2015) Jupiter's Deep Cloud Structure Revealed Using Keck Observations of Spectrally Resolved Line Shapes. The Astrophysical Journal 810, 122 (10 pp.). (<https://ui.adsabs.harvard.edu/abs/2015ApJ...810..122B>)

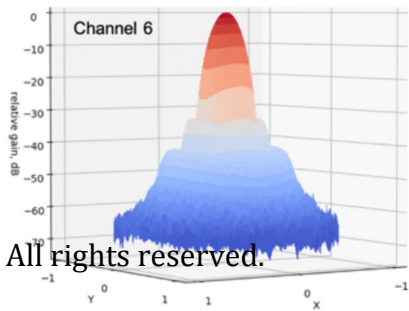
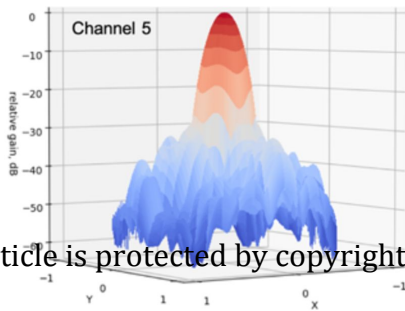
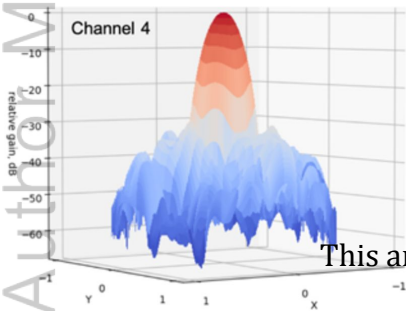
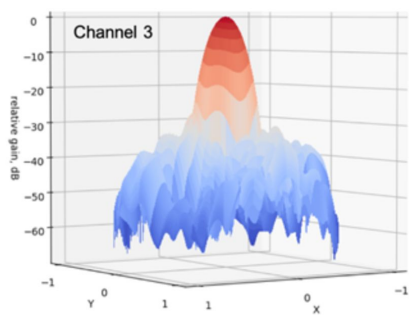
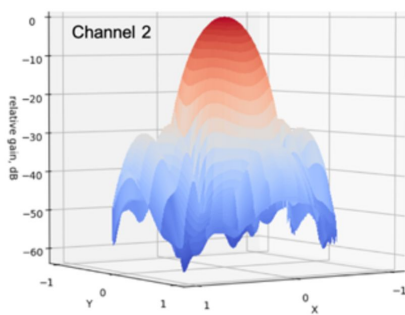
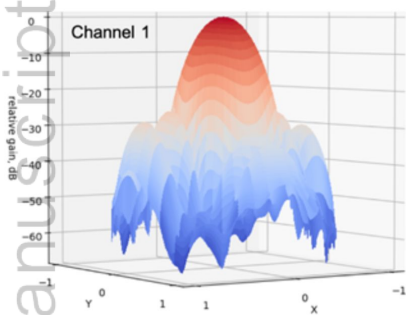
591 Bjoraker, G. L., H. P. Larson, and V. G. Kunde (1986) The Abundance and Distribution of Water Vapor in Jupiter's
592 Atmosphere. *The Astrophysical Journal* 311, 1058–1072.
593
594
595 Bolton, S. J., Lunine, J., Stevenson, D., Connerney, J. E. P., Levin, S., Owen, T. C., Bagenal, F., Gautier, D., Ingersoll,
596 A. P., Orton, G. S., Guillot, T., Hubbard, W., Bloxham, J., Coradini, A., Stephens, S. K., Mokashi, P., Thorne,
597 R., Thorpe, R., The Juno Mission, *Space Science Reviews*, Volume 213, pp. 5-37, 2017.
598
599 Bolton, S. J., The deep structure of Jupiter's winds and cyclones. 2020
600
601 Burke, B. F., and K. L. Franklin (1955) Observations of a variable radio source associated with the planet Jupiter, *J.*
602 *Geophys. Res.*, 60, 213–217.
603
604
605 de Pater, I., and S. T. Massie, Models of the millimeter-centimeter spectra of the giant planets, *Icarus* 62, 143–171,
606 1985.
607
608 de Pater, I., D. Dunn, P. Romani, and K. Zahnle, Reconciling Galileo probe data and ground-based radio
609 observations of ammonia on Jupiter, *Icarus* 149, 66–78, 2001.
610
611 de Pater, I., Sault, R.J., Butler, B., DeBoer, D., Wong, M.H., Peering through Jupiter's clouds with radio spectral
612 imaging. *Science* 2016, June, 03. Vol. 352, Issue 6290, pp. 1198-1201. DOI: 10.1126/science.aaf2210
613
614 de Pater, I., Sault, R. J., Wong, M. H., Fletcher, L.N., DeBoer, D., Butler, B. (2019) Jupiter's ammonia distribution
615 derived from VLA aps at 3–37 GHz. *Icarus* 322, 168-191. doi: 10:1016/j.icarus.2018.11.024
616
617 de Pater et al. 2019. Jupiter's ammonia distribution derived from VLA maps at 3–37 GHz. *Icarus* 322; 168–191
618
619 Fletcher, L. N., Orton, G. S., Yanamandra-Fisher, P., Fisher, B. M., Parrish, P. D., Irwin, P. G. J.. Retrievals of
620 atmospheric variables on the gas giants from ground-based mid-infrared imaging, *Icarus* 200, 154–175, 2009.
621
622 Fletcher, L.N., Orton, G.S., Greathouse, T.K., Rogers, J.H., Zhang, Z., Oyafuso, F.A., Eichstadt, G., Melin, H., Li,
623 C., Levin, S.M., Bolton, S., Janssen, M., Metting, H.-J., Grassi, D., Mura, A., Adriani, A., Jupiter's Equatorial
624 Plumes and Hot Spots: Spectral Mapping from Gemini/TEXES and Juno/MWR. *JGR Planets* 2020,
625 10.1029/2020JE006399.
626
627 Folkner, W. M., R. Woo, and S. Nandi, Ammonia abundance in Jupiter's atmosphere derived from the attenuation of
628 the Galileo probe's radio signal, *J. Geophys. Res.*, 103, 22847–22856, 1998.
629
630 Fouchet, T., E. Lellouch, B. B  lezard, T. Encrenaz, P. Drossart, H. Feuchtgruber, and T. de Graauw, ISO-SWS
631 Observations of Jupiter: Measurement of the Ammonia Tropospheric Profile and of the ¹⁵N/¹⁴N Isotopic Ratio,
632 *Icarus* 143, 223–243, 2000.
633
634 Grassi, D., A. Adriani, A. Mura, B. M. Dinelli, G. Sindoni, D. Turrini, G. Filacchione, A. Migliorini, M. L.
635 Moriconi, F. Tosi, R. Noschese, A. Cicchetti, F. Altieri, F. Fabiano, G. Piccioni, S. Stefani, S. Atreya, J. Lunine, G.
636 Orton, A. Ingersoll, S. Bolton, S. Levin, J. Connerney, A. Olivieri, and M. Amoroso (2017) Preliminary results on
637 the composition of Jupiter's troposphere in hot spot regions from the JIRAM/Juno instrument. *Geophysical Research*
638 *Letters* 44, 4615–4624. (<https://ui.adsabs.harvard.edu/abs/2017GeoRL..44.4615G>)
639
640 Helled, R.,; and Lunine, J., Measuring Jupiter's water abundance by Juno: the link between interior and formation
641 models, *Monthly Notices of the Royal Astronomical Society*, Volume 441, Issue 3, p.2273-2279, 2014.
642
643 Ingersoll, Andrew P., Adumitroaie, Virgil, Allison, Michael D., Atreya, Sushil, Bellotti, Amadeo A., Bolton, Scott J.
644 , Brown, Shannon T., Gulkis, Samuel, Janssen, Michael A., Levin, Steven M., Li, Cheng, Li, Liming, Lunine, Jonathan
645 an I., Orton, Glenn S., Oyafuso, Fabiano A., and Steffes, Paul G., Implications of the ammonia distribution

646 on Jupiter from 1 to 100 bars as measured by the Juno microwave radiometer, *Geophysical Research Letters*,
647 Volume 44, Issue 15, pp. 7676-7685, 2017.
648
649 Janssen, M. A.; Oswald, J. E.; Brown, S. T.; Gulkis, S.; Levin, S. M.; Bolton, S. J.; Allison, M. D.; Atreya, S. K.; Ga
650 utier, D.; Ingersoll, A. P.; Lunine, J. I.; Orton, G. S.; Owen, T. C.; Steffes, P. G.; Adumitroaie, V.; Bellotti, A.; Jewel
651 l, L. A.; Li, C.; Li, L.; Misra, S.; Oyafuso, F. A.; Santos
652 Costa, D.; Sarkissian, E.; Williamson, R.; Arballo, J. K.; Kitiyakara, A.; Ulloa
653 Severino, A.; Chen, J. C.; Maiwald, F. W.; Sahakian, A. S.; Pingree, P. J.; Lee, K. A.; Mazer, A. S.; Redick, R.; Hod
654 ges, R. E.; Hughes, R. C.; Bedrosian, G.; Dawson, D. E.; Hatch, W. A.; Russell, D. S.; Chamberlain, N. F.; Zawadsk
655 i, M. S.; Khayatian, B.; Franklin, B. R.; Conley, H. A.; Kempenaar, J. G.; Loo, M. S.; Sunada, E. T.; Vorperion, V.;
656 Wang, C. C. MWR: Microwave Radiometer for the Juno Mission to Jupiter. *Space Science Reviews*, Volume 213,
657 Issue 1-4, pp. 139-185, 2017.
658
659 Janssen, M. A. Book: Atmospheric remote sensing by microwave radiometer. Wiley-Interscience publication, 1993.
660
661 Kunde, V., R. Hanel, W. Maguire, D. Gautier, J. P. Baluteau, A. Marten, A. Chedin, N. Husson, and N. Scott, The
662 tropospheric gas composition of Jupiter's north equatorial belt NH₃, PH₃, CH₃D, GeH₄, H₂O and the Jovian D/H
663 isotopic ratio, *ApJ* 263, 443–467, 1982.
664
665 Li, Cheng; Ingersoll, Andrew; Janssen, Michael; Levin, Steven; Bolton, Scott; Adumitroaie, Virgil; Allison, Michael
666 ; Arballo, John; Bellotti, Amadeo; Brown, Shannon; Ewald, Shawn; Jewell, Laura; Misra, Sidharth; Orton, Glenn; O
667 yafuso, Fabiano; Steffes, Paul; Williamson, Ross. The distribution of ammonia on Jupiter from a preliminary
668 inversion of Juno microwave radiometer data. *Geophysical Research Letters*, Volume 44, Issue 11, pp. 5317-5325,
669 2017.
670
671 Li, C., A. Ingersoll, S. Bolton, S. Levin, M. Janssen, S. Atreya, J. Lunine, P. Steffes, S. Brown, T. Guillot, M.
672 Allison, J. Arballo, A. Bellotti V. Adumitroaie, S. Gulkis, A. Hodges, L. Li, S. Misra, G. Orton, F. Oyafuso, D.
673 Santos-Costa, H. Waite, and Z. Zhang, "The water abundance in Jupiter's equatorial zone," *Nature Astronomy*,
674 vol.4, published February 10, 2020. (doi: 10.1038/s41550-020-1009-3).
675
676 Oyafuso, F. A. et al., Positional and angular dependence of Jupiter's thermal emission: analysis from Juno's
677 Microwave Radiometer. 2020
678
679 Rohlfs, K., Wilson, T. Book: Tools of radio astronomy 3rd Edition, 1999.
680
681 Santos-Costa, D., V. Adumitroaie, A. Ingersoll, S. Gulkis, M. A. Janssen, S. M. Levin, F. Oyafuso, S. Brown, R.
682 Williamson, S. J. Bolton, and J. E. P. Connerney (2017) First look at Jupiter's synchrotron emission from Juno's
683 perspective. *Geophysical Research Letters* 44, 8676–8684.
684 (<https://ui.adsabs.harvard.edu/abs/2017GeoRL..44.8676S>)
685
686 Sromovsky, L. A., A. D. Collard, P. M. Fry, G. S. Orton, M. T. Lemmon, M. G. Tomasko, and R. S. Freedman,
687 Galileo probe measurements of thermal and solar radiation fluxes in the Jovian atmosphere, *J. Geophys. Res.* 103,
688 22,929–22,978, 1998.
689
690 Taylor, F. W., Atreya, S. K., Encrenaz, Th., Hunten, D. M., Irwin, P. G. J., Owen, T. C. The composition of the
691 atmosphere of Jupiter. *Jupiter*, Cambridge University Press, 2007, p.59. 2007jupi.book...59T
692
693 V Adumitroaie et al. "Towards a fast background radiation subtraction technique for the Juno mission". In:
2016 IEEE Aerospace Conference (2016), pp. 1–11.
694
695 Wong, M. H., P. R. Mahaffy, S. K. Atreya et al. (2004), Updated Galileo probe mass spectrometer measurements of
696 carbon, oxygen, nitrogen, and sulfur on Jupiter, *Icarus*, 171, 153–170.

- 697 Hanley, T. R., P. G. Steffes, and B. M. Karpowicz (2009) A new model of the hydrogen and helium-broadened
698 microwave opacity of ammonia based on extensive laboratory measurements. *Icarus* 202, 316–335.
699
- 700 Zhang, Zhimeng, Adumitroaie, Virgil, Allison, Michael, Arballo, John, Atreya, Sushil, Bjoraker, Gordon, ...
701 Wong, Michael. (2020). Dataset for Residual Study: Testing Jupiter Atmosphere Models Against Juno MWR
702 Observations [Data set]. Zenodo. <http://doi.org/10.5281/zenodo.3723462>

Figure1.

Author Manuscript

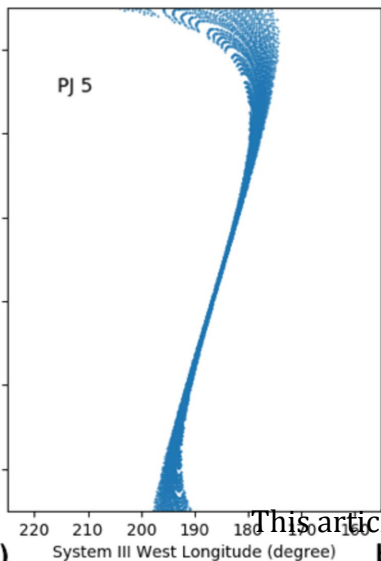


This article is protected by copyright. All rights reserved.

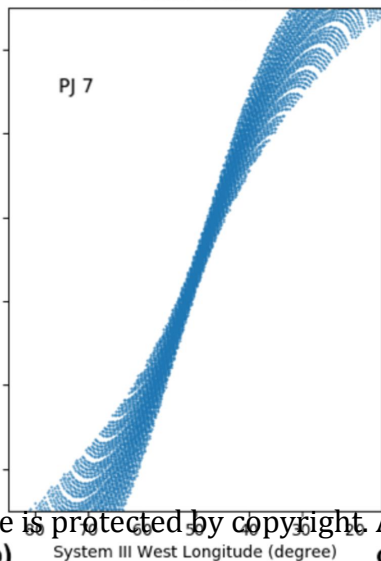
Figure2.

Author Manuscript

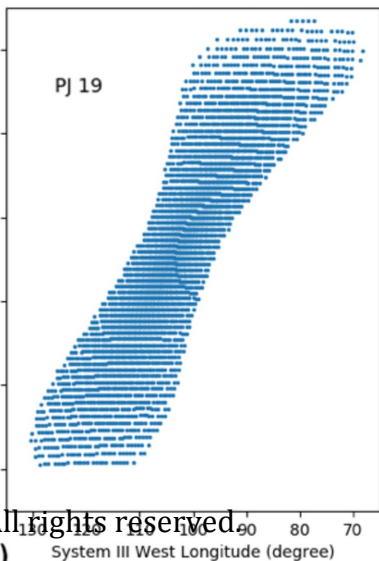
MWR Tilt Orbit



MWR Orbit



MWR Cross-track Orbit



This article is protected by copyright. All rights reserved.

Figure3.

Author Manuscript

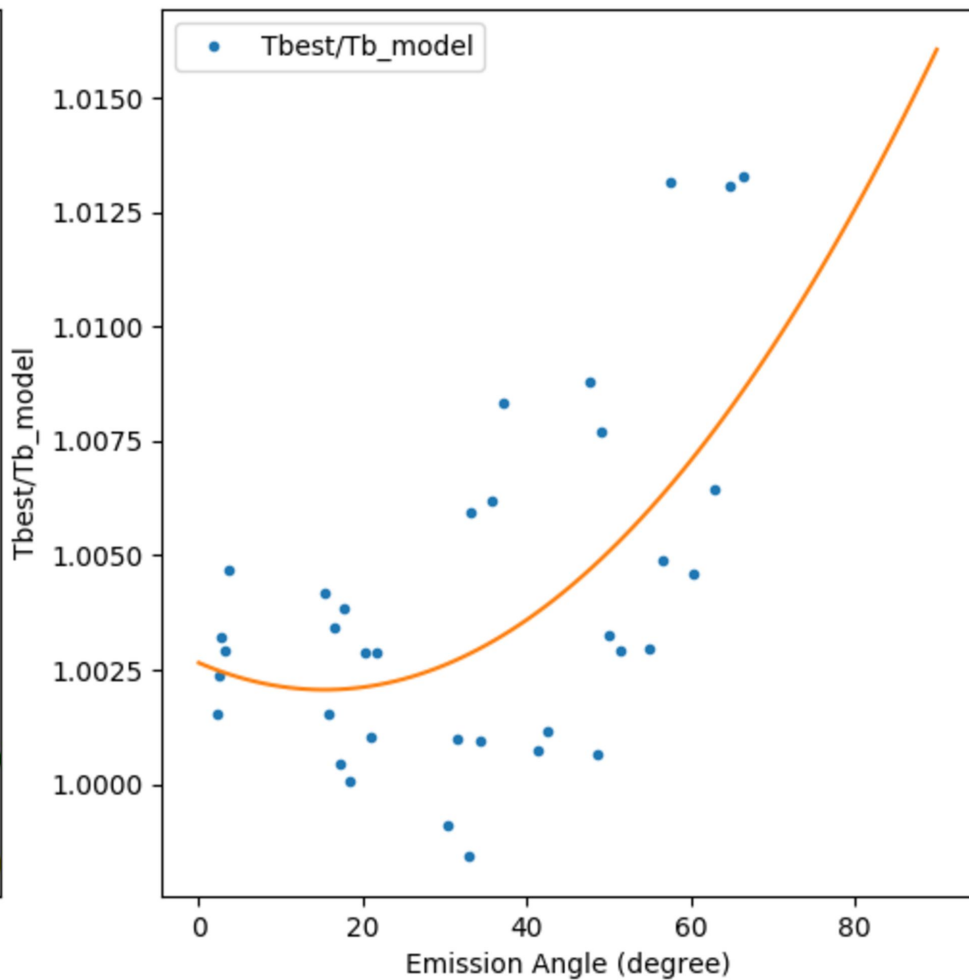
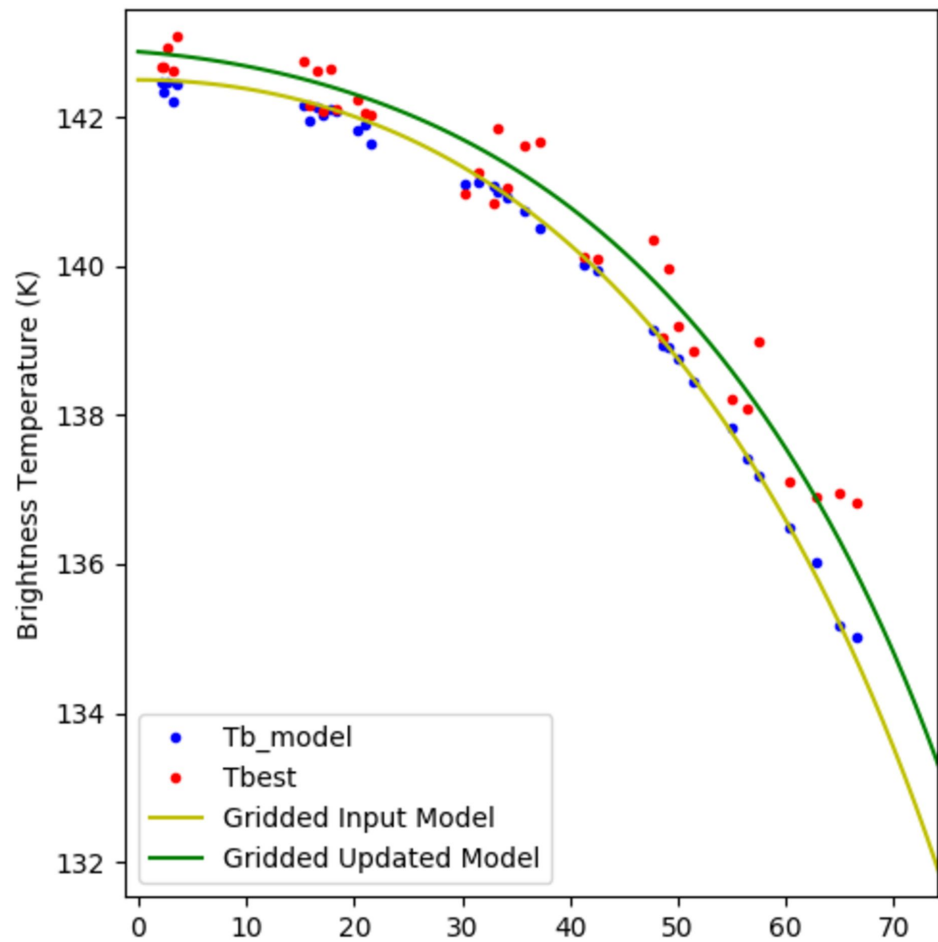
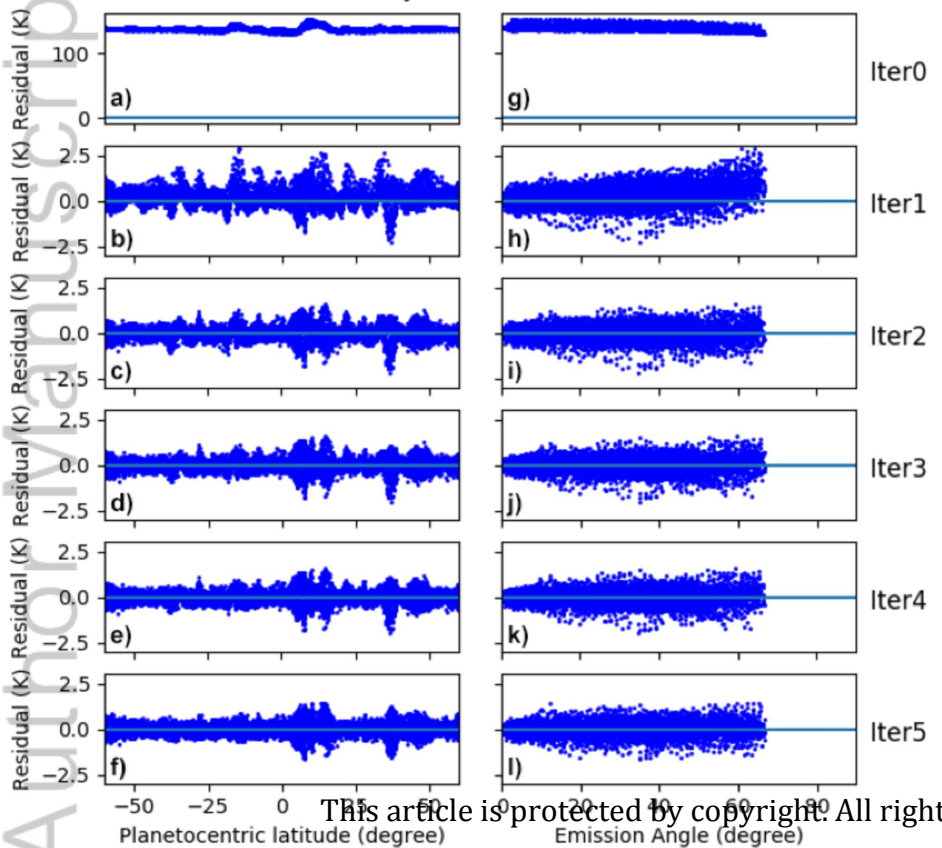


Figure4.

Author Manuscript

PJ1 Channel 6



This article is protected by copyright. All rights reserved.

Figure5.

Author Manuscript

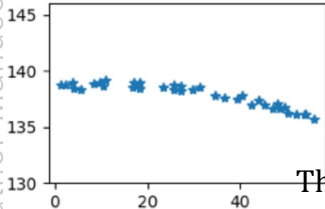
PJ1 Channel 6

30°S Lat

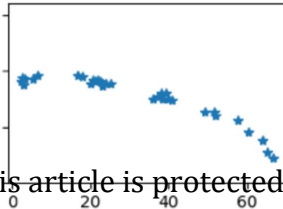
0° Lat

15°N Lat

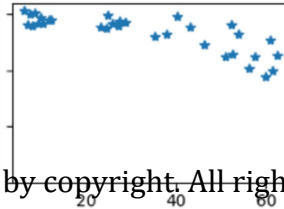
30°N Lat

**a)**

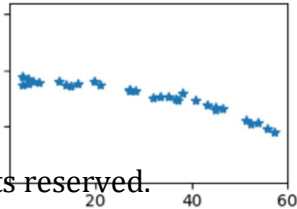
Emission Angle (degree)

**b)**

Emission Angle (degree)

**c)**

Emission Angle (degree)

**d)**

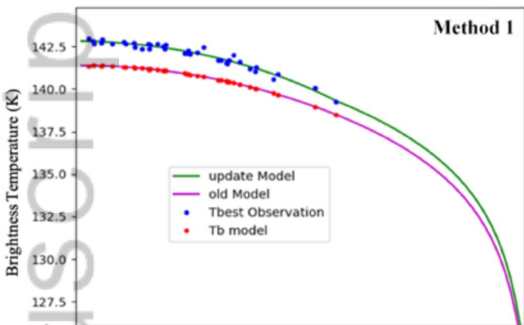
Emission Angle (degree)

This article is protected by copyright. All rights reserved.

Figure6.

Author Manuscript

70°S Latitude



0° Latitude

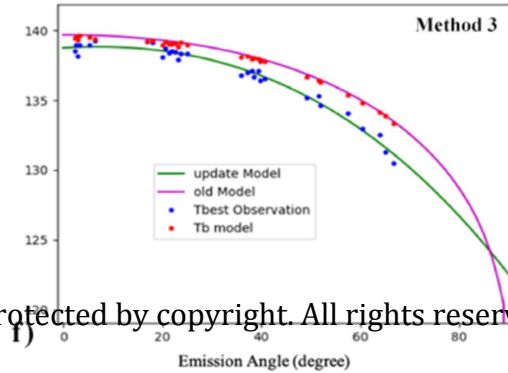
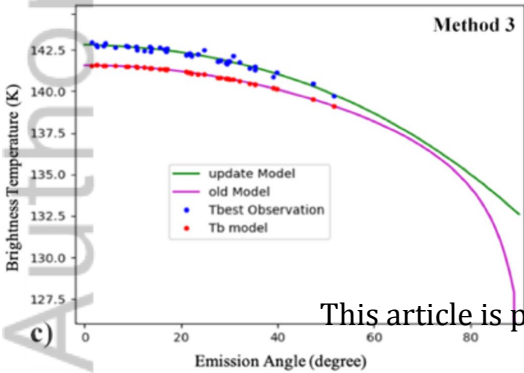
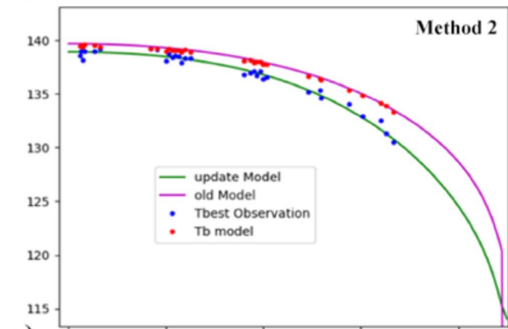
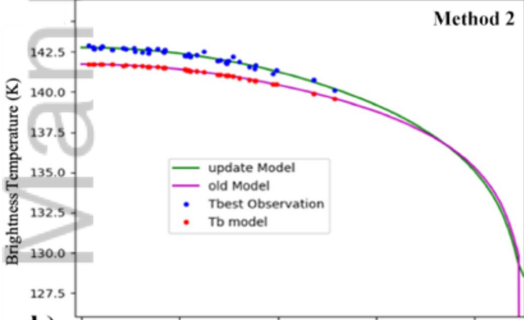
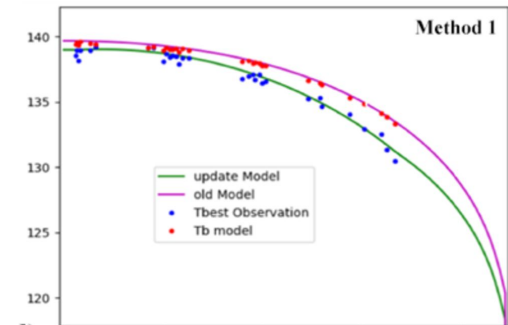
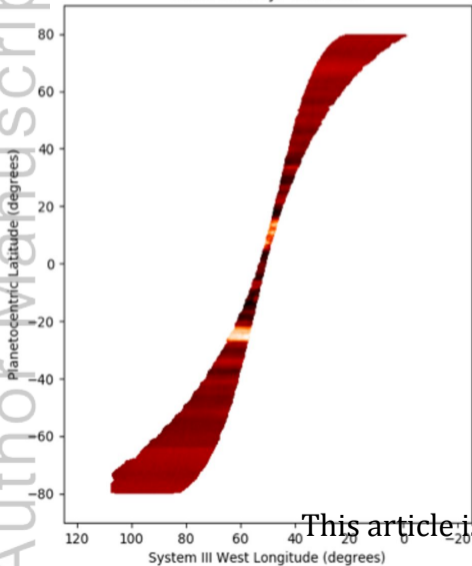


Figure 7.

Author Manuscript

MWR Orbit PJ7 Channel6



MWR Orbit PJ7 Channel6

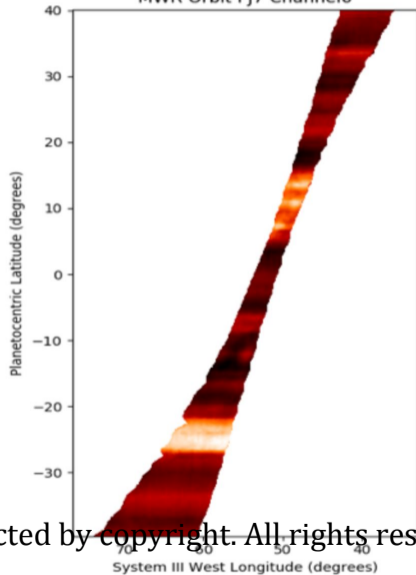


Figure8.

Author Manuscript

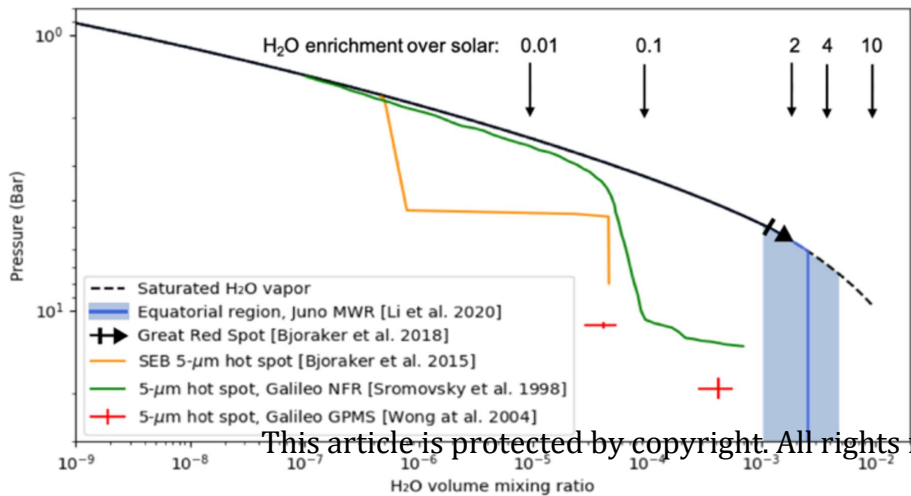


Figure9.

Author Manuscript

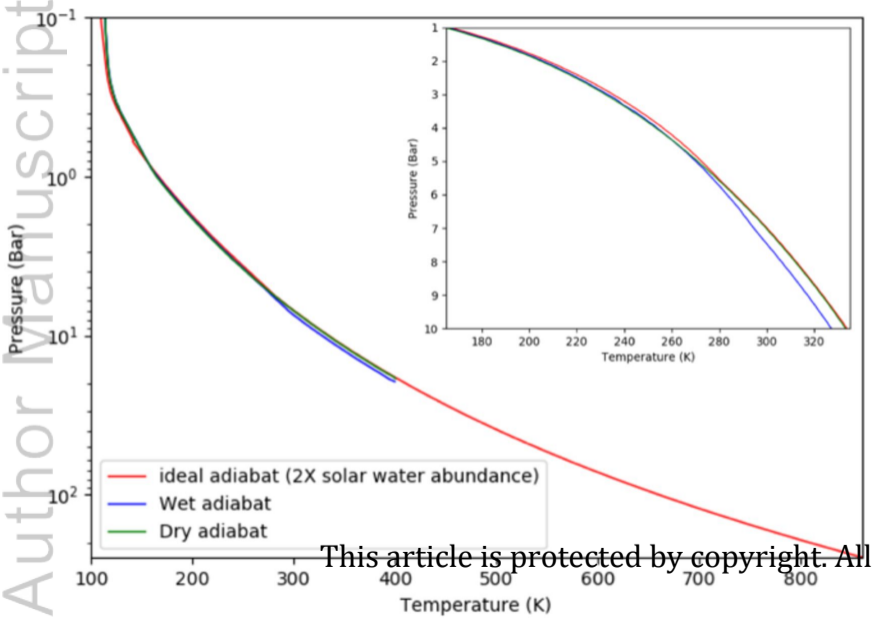
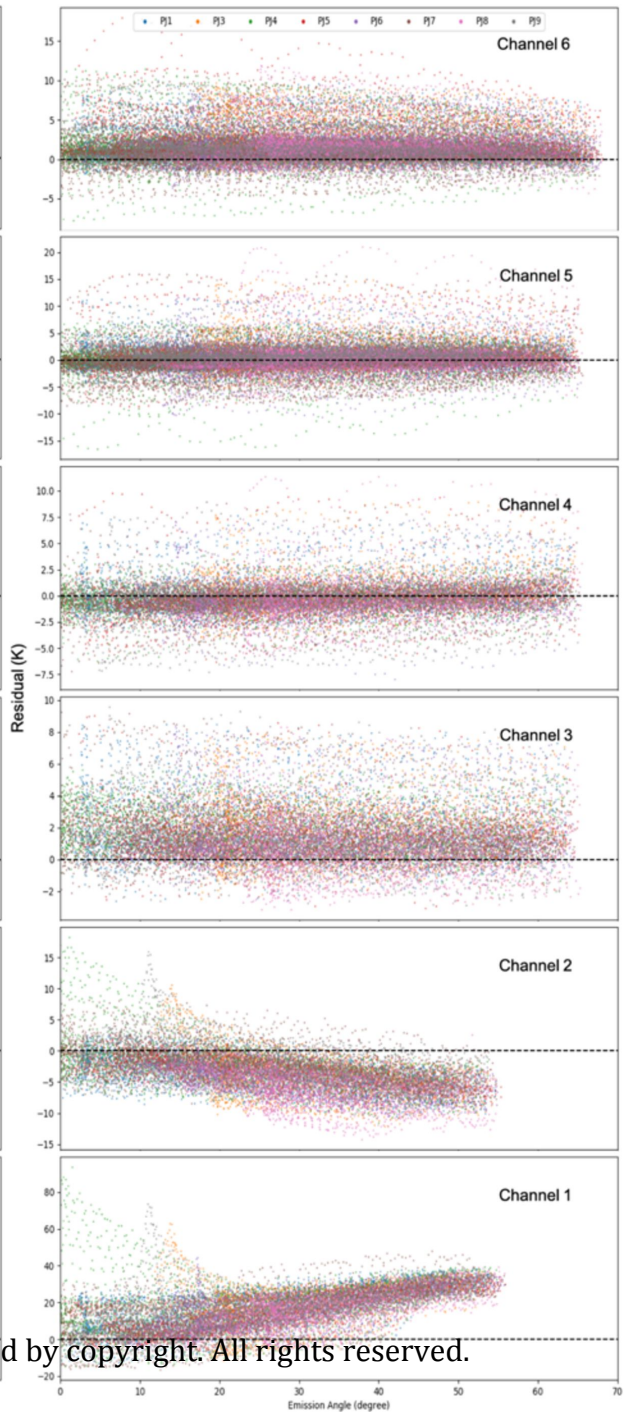
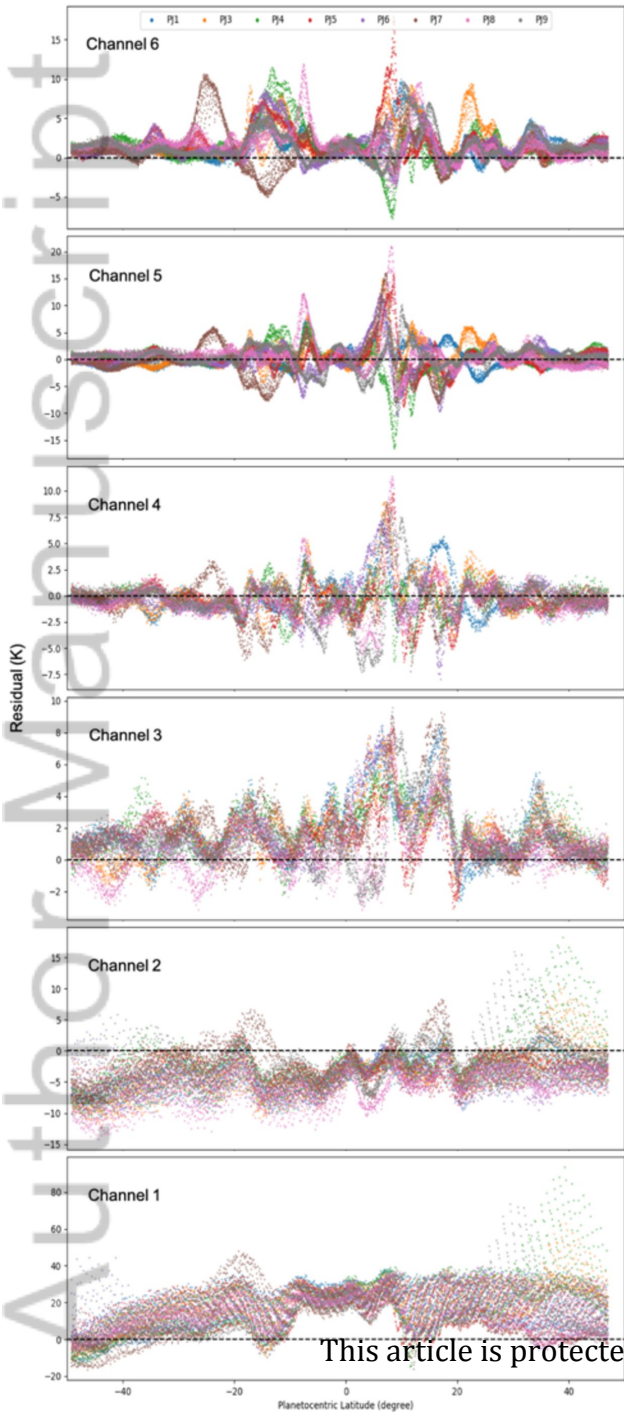


Figure10.

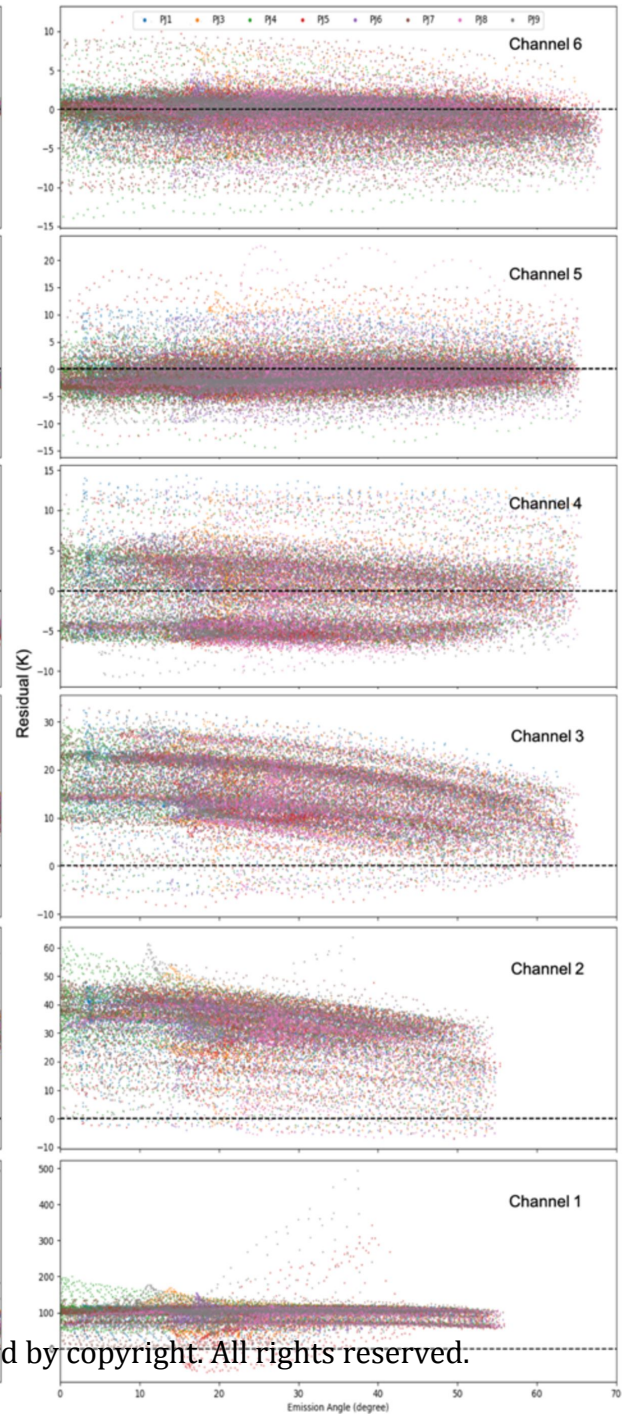
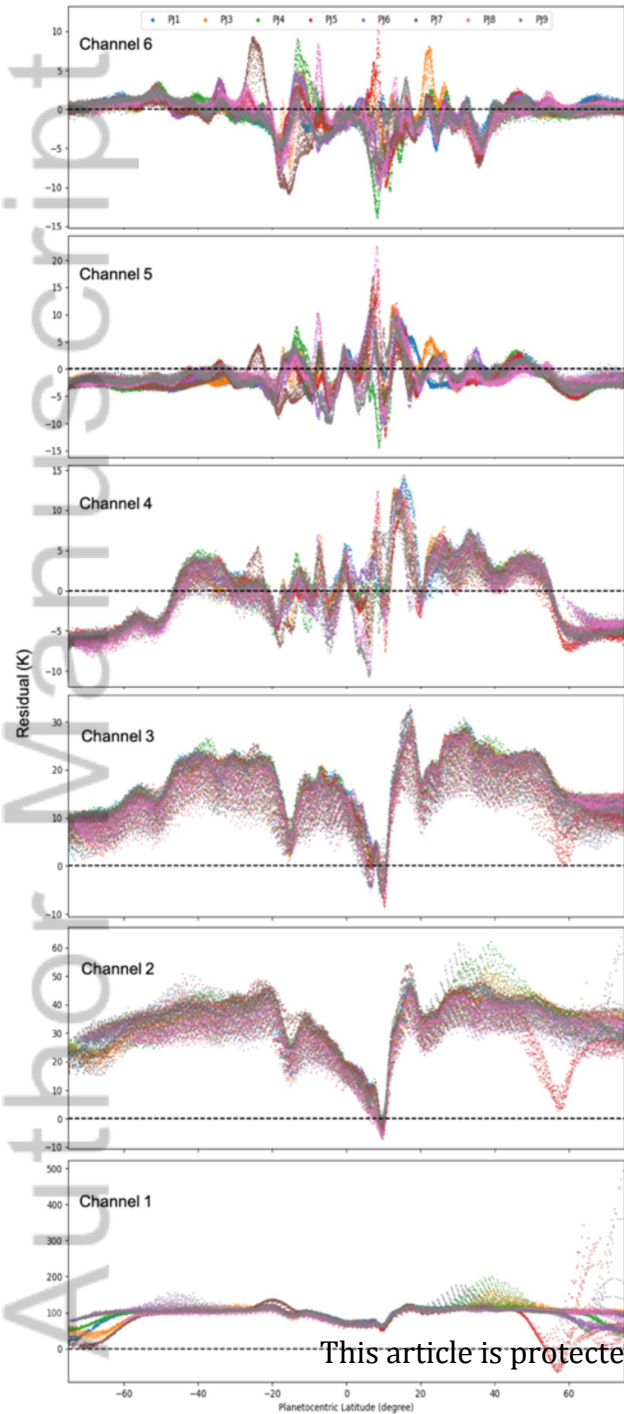
Author Manuscript



This article is protected by copyright. All rights reserved.

Figure11.

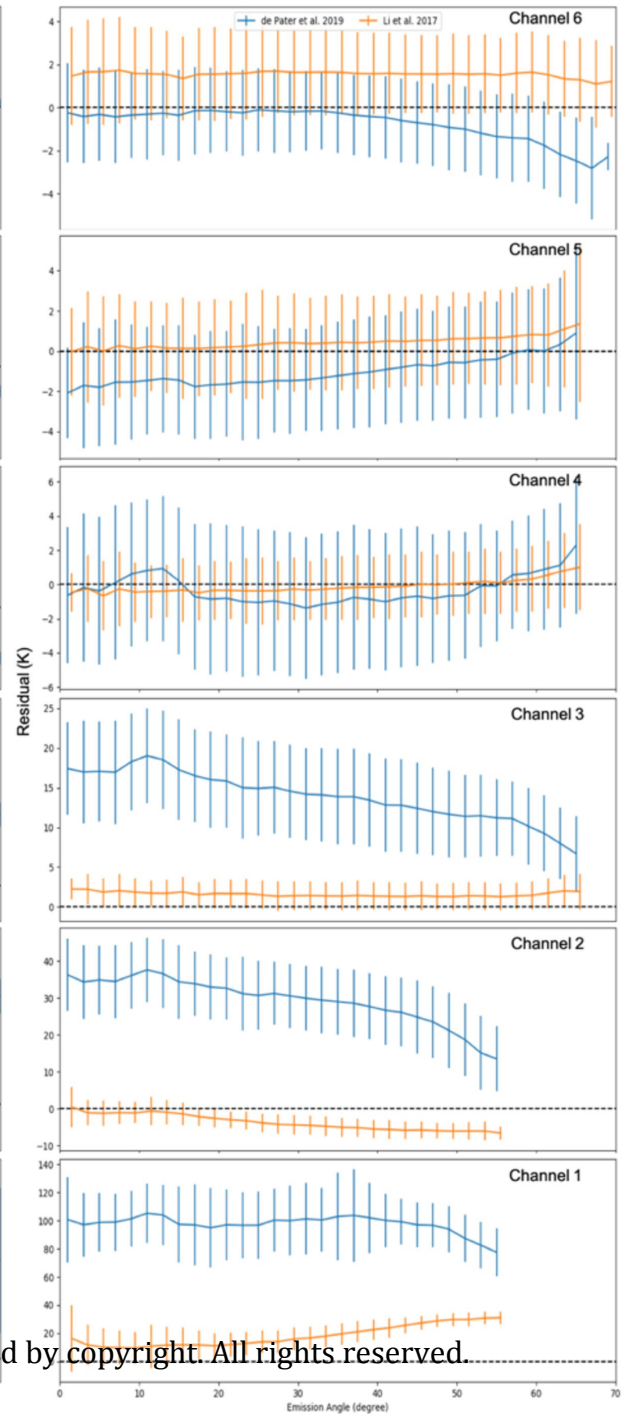
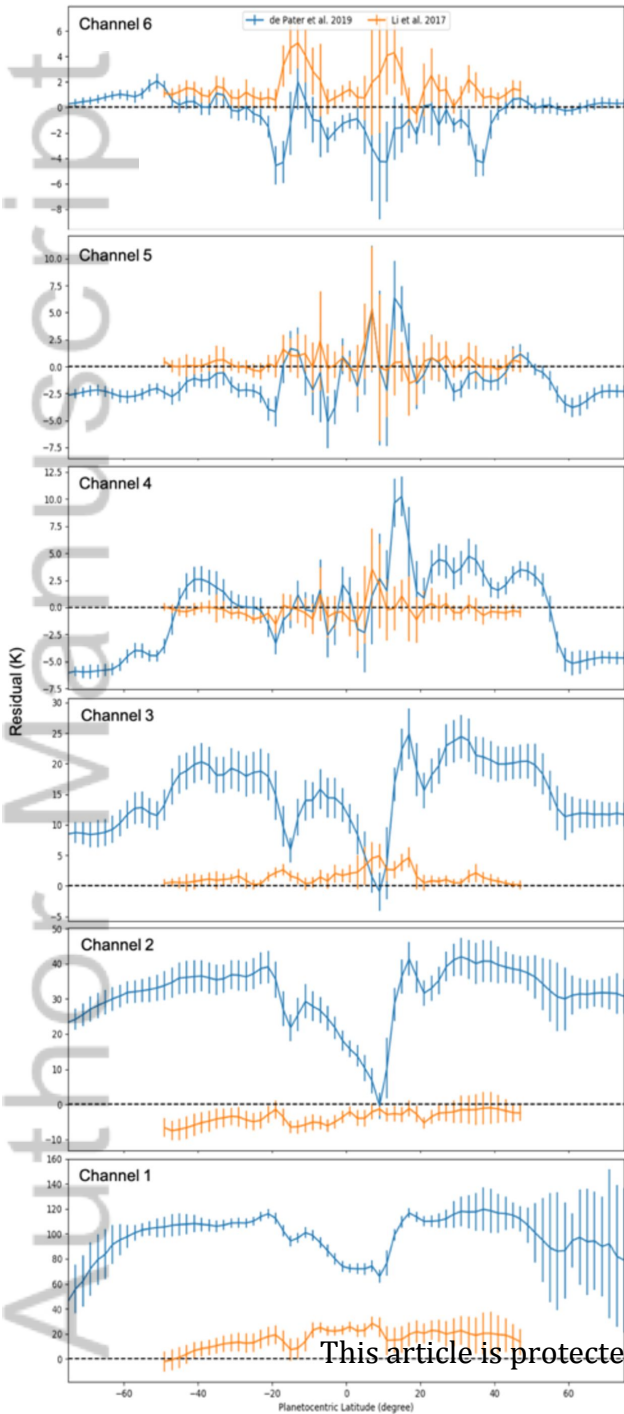
Author Manuscript



This article is protected by copyright. All rights reserved.

Figure12.

Author Manuscript



This article is protected by copyright. All rights reserved.

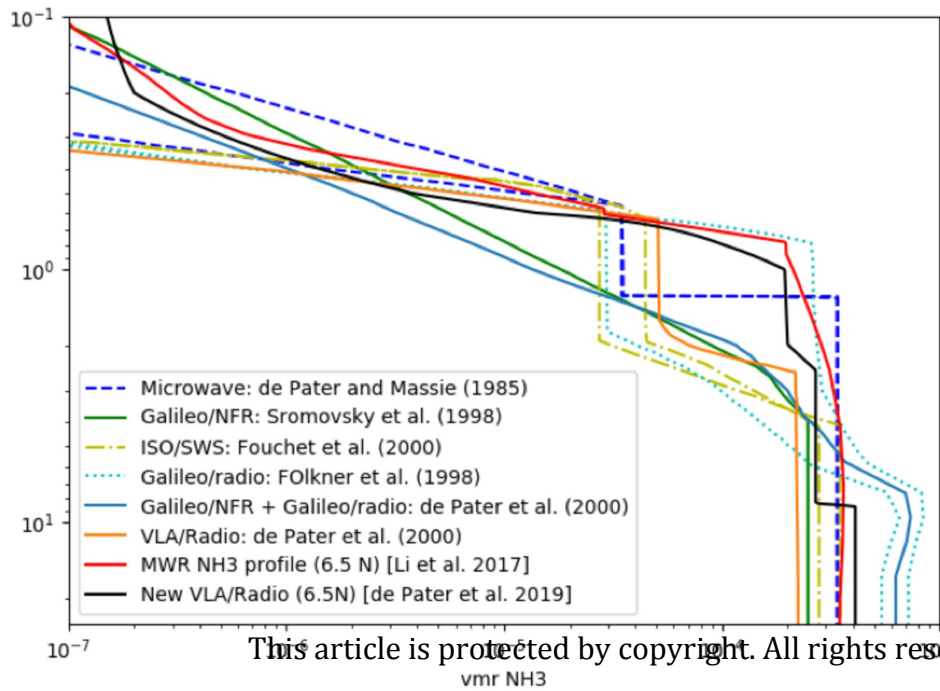
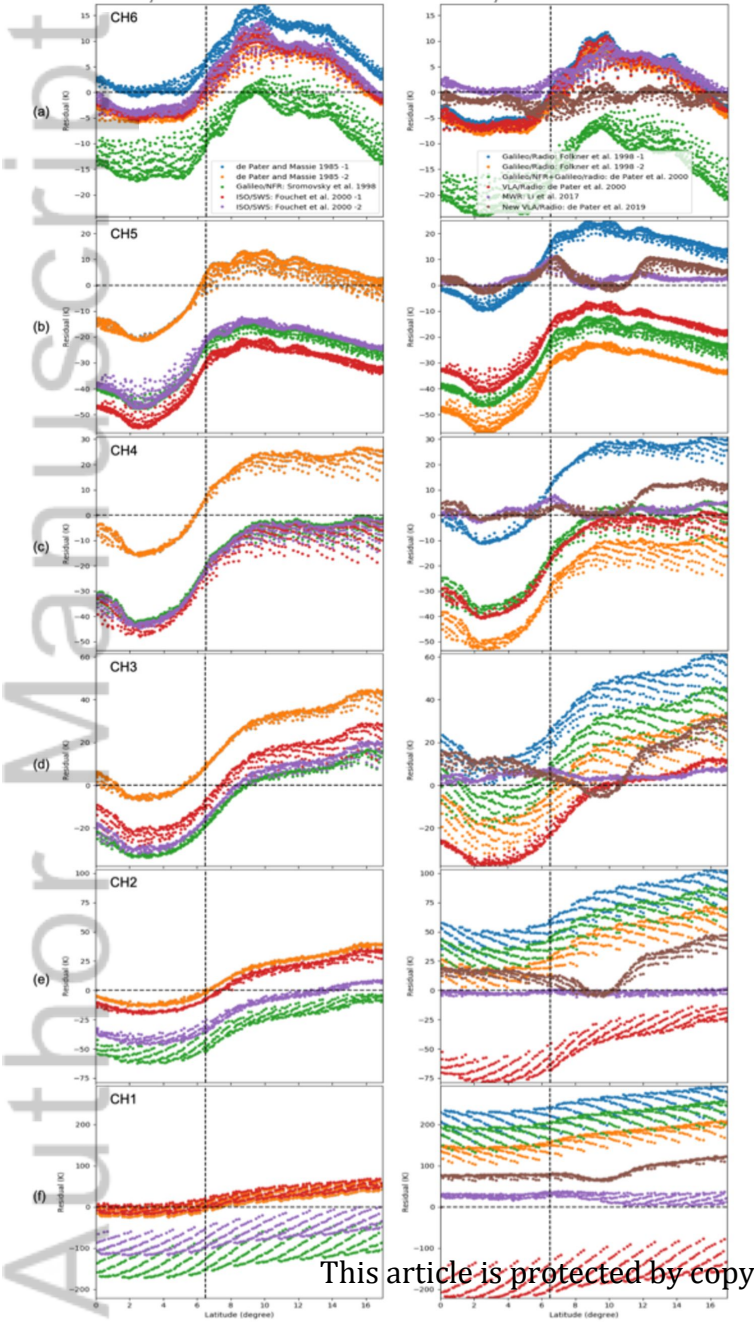
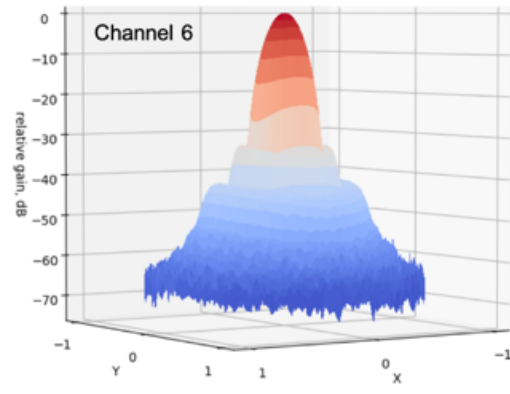
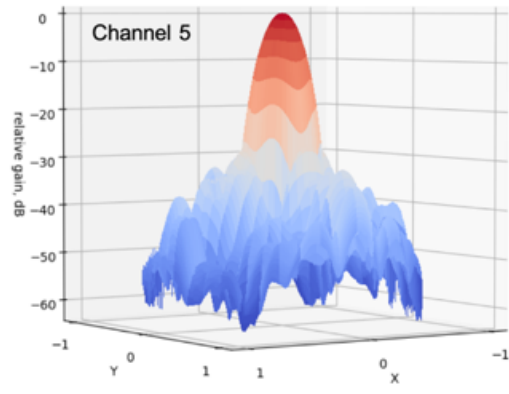
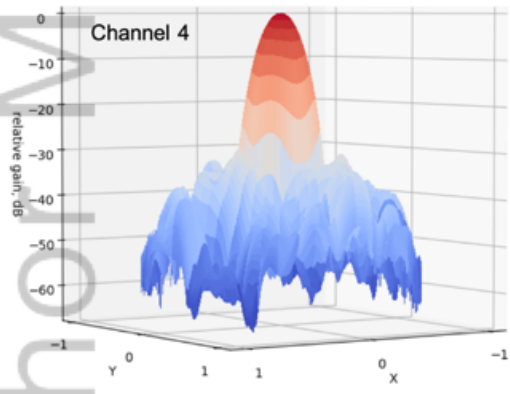
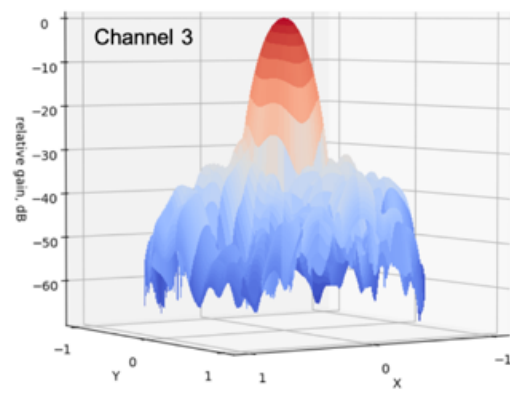
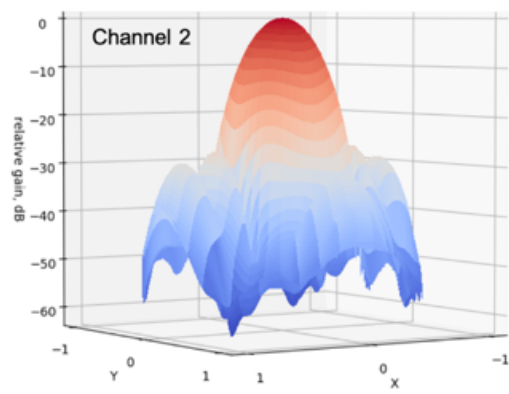
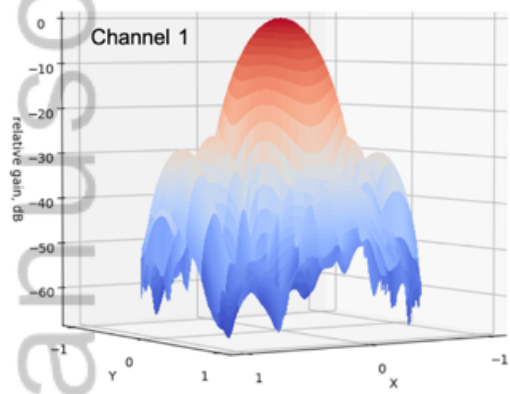


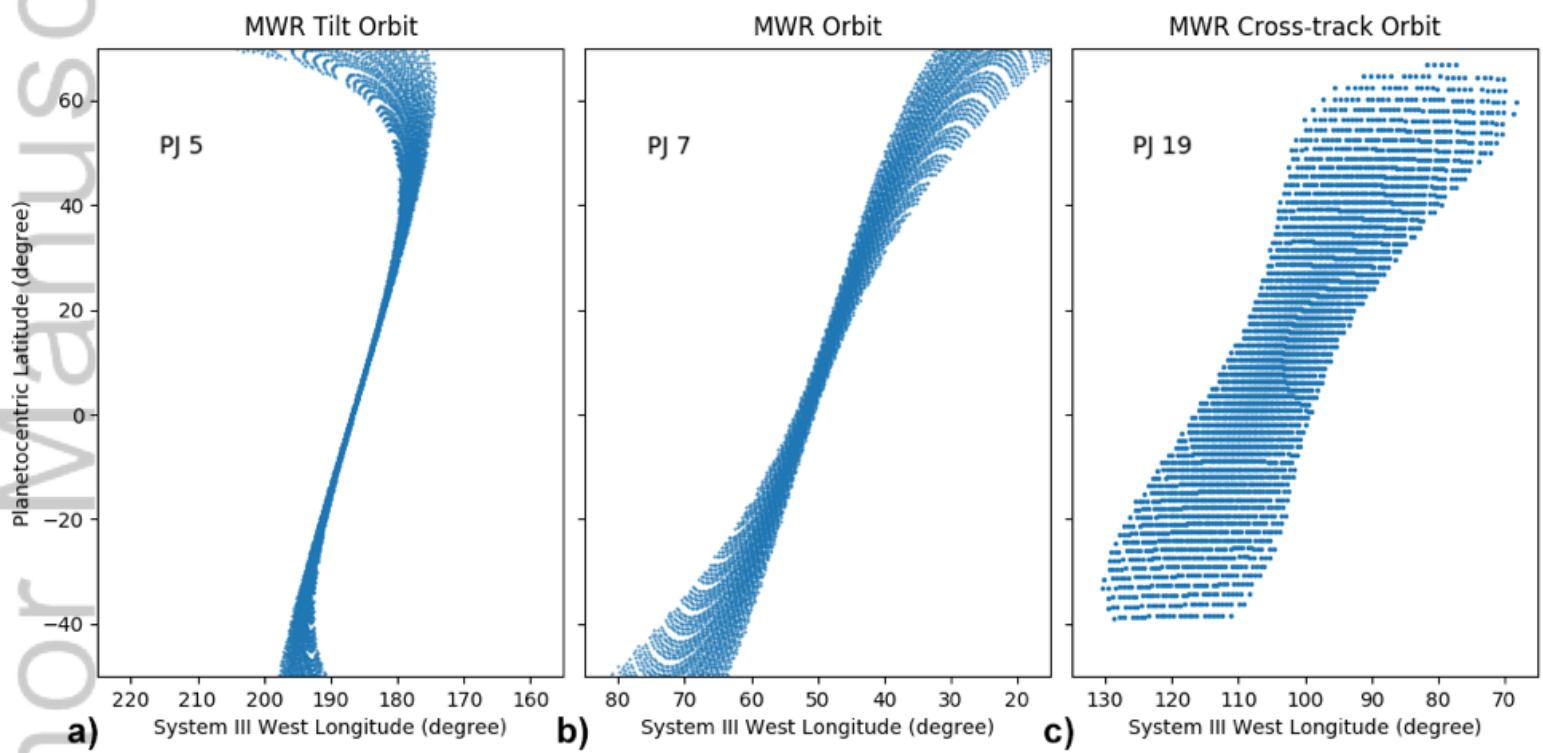
Figure14.

Author Manuscript

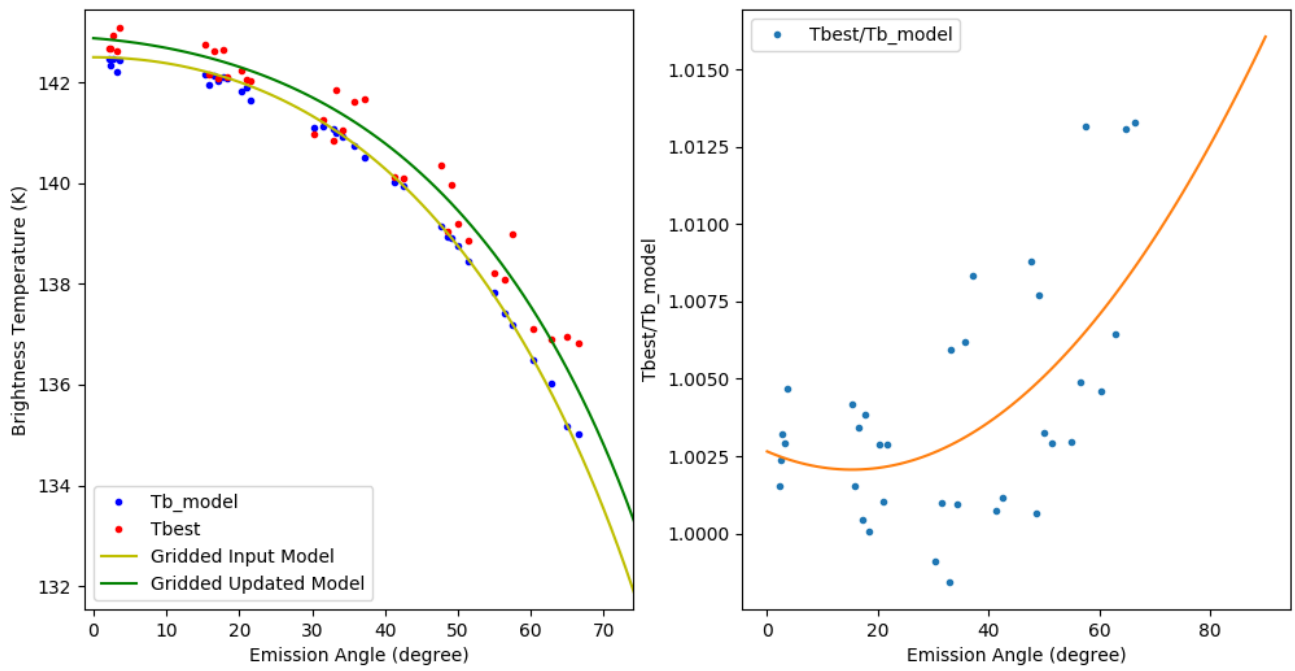




ESS2_634_2020EA001229-f01-z-.png

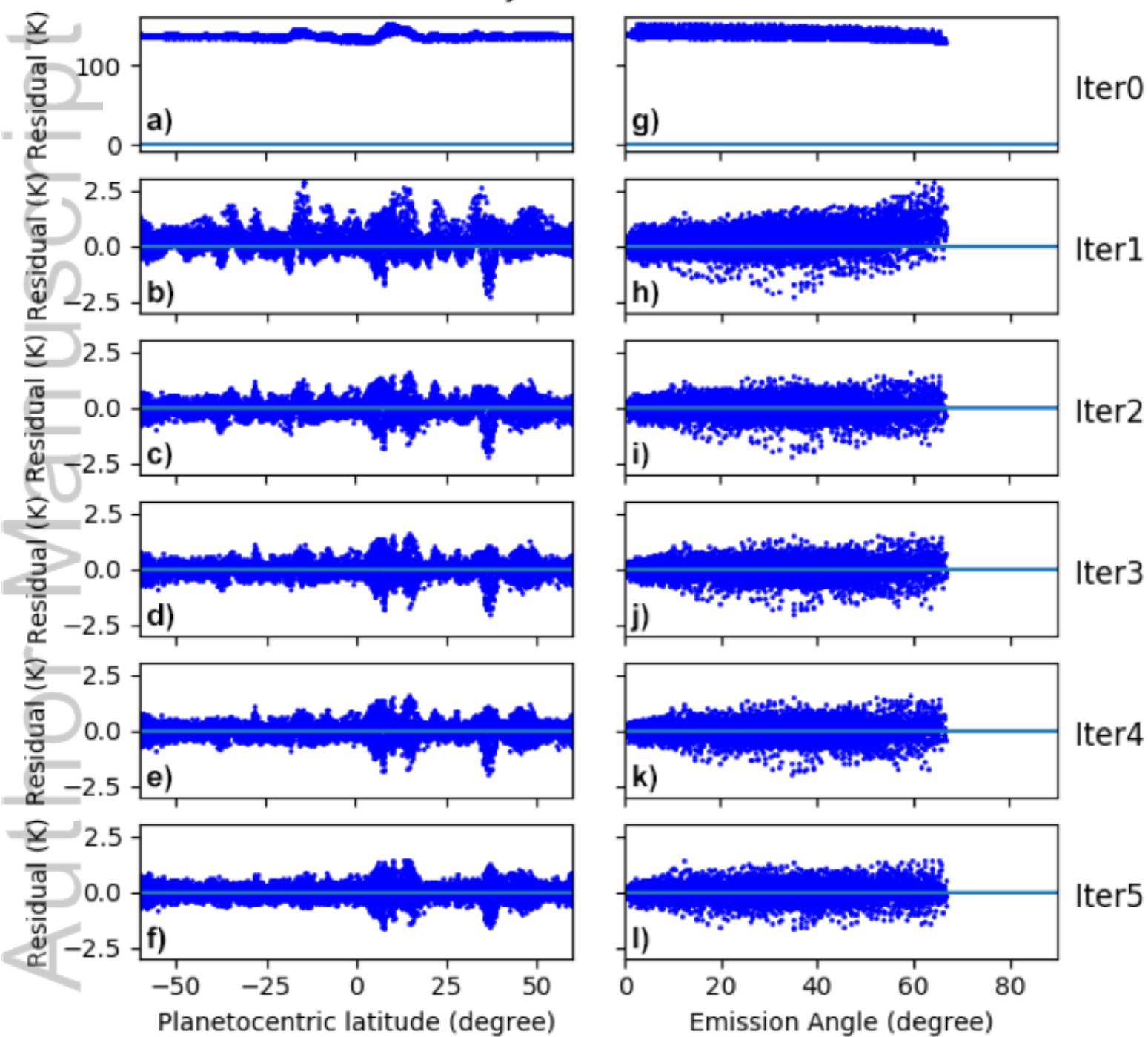


ESS2_634_2020EA001229-f02-z-.png

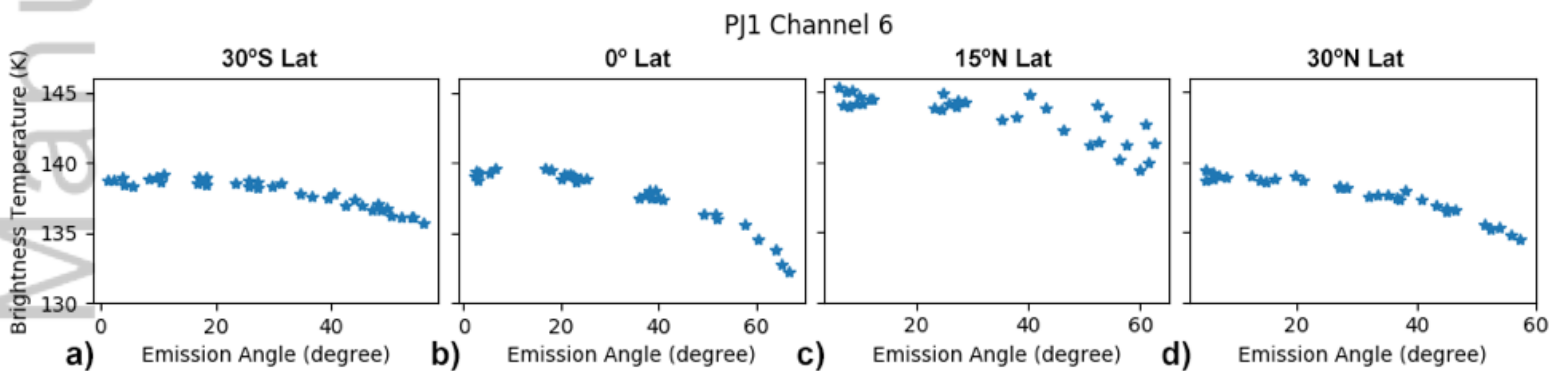


ESS2_634_2020EA001229-f03-z-.png

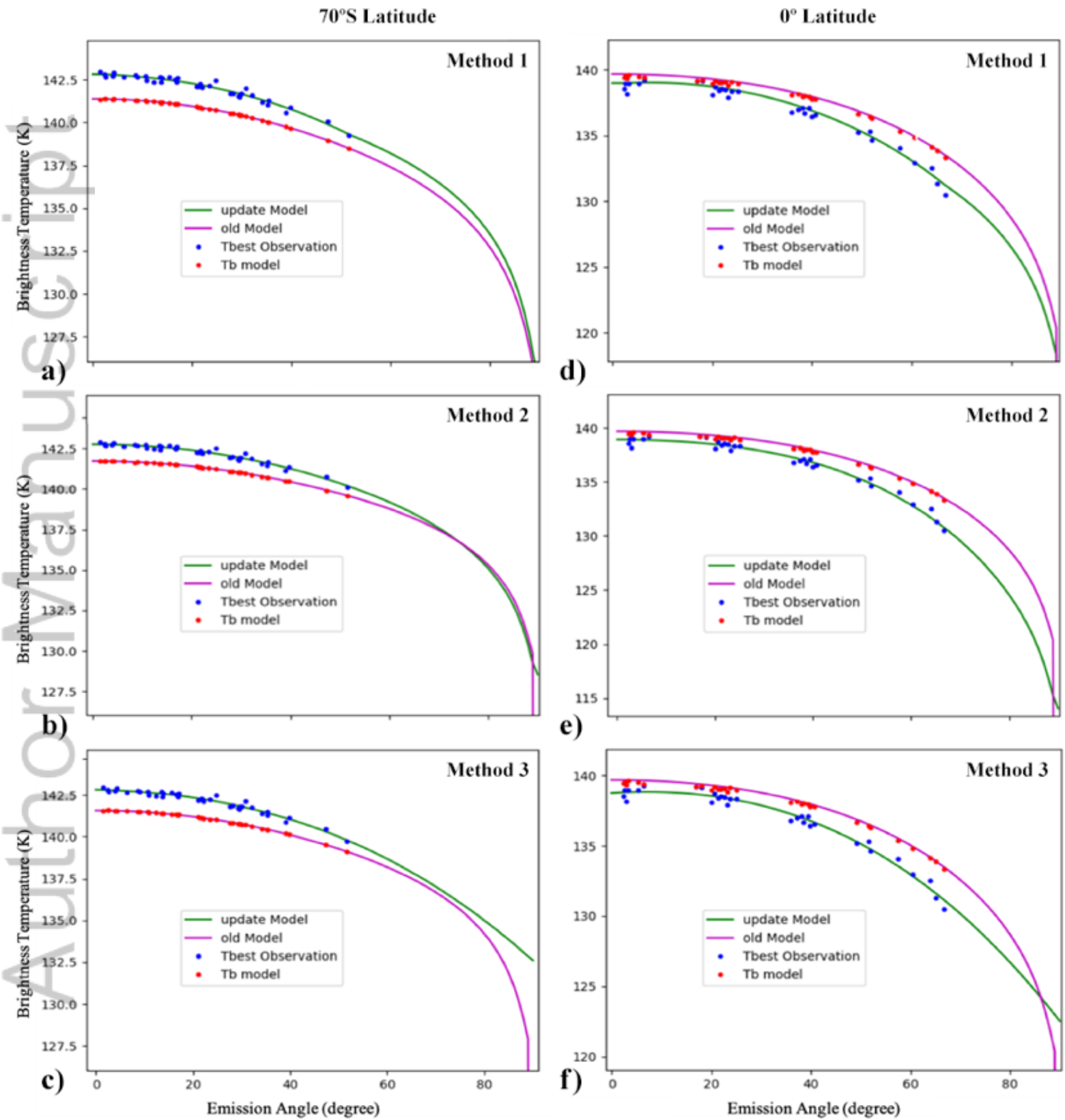
PJ1 Channel 6



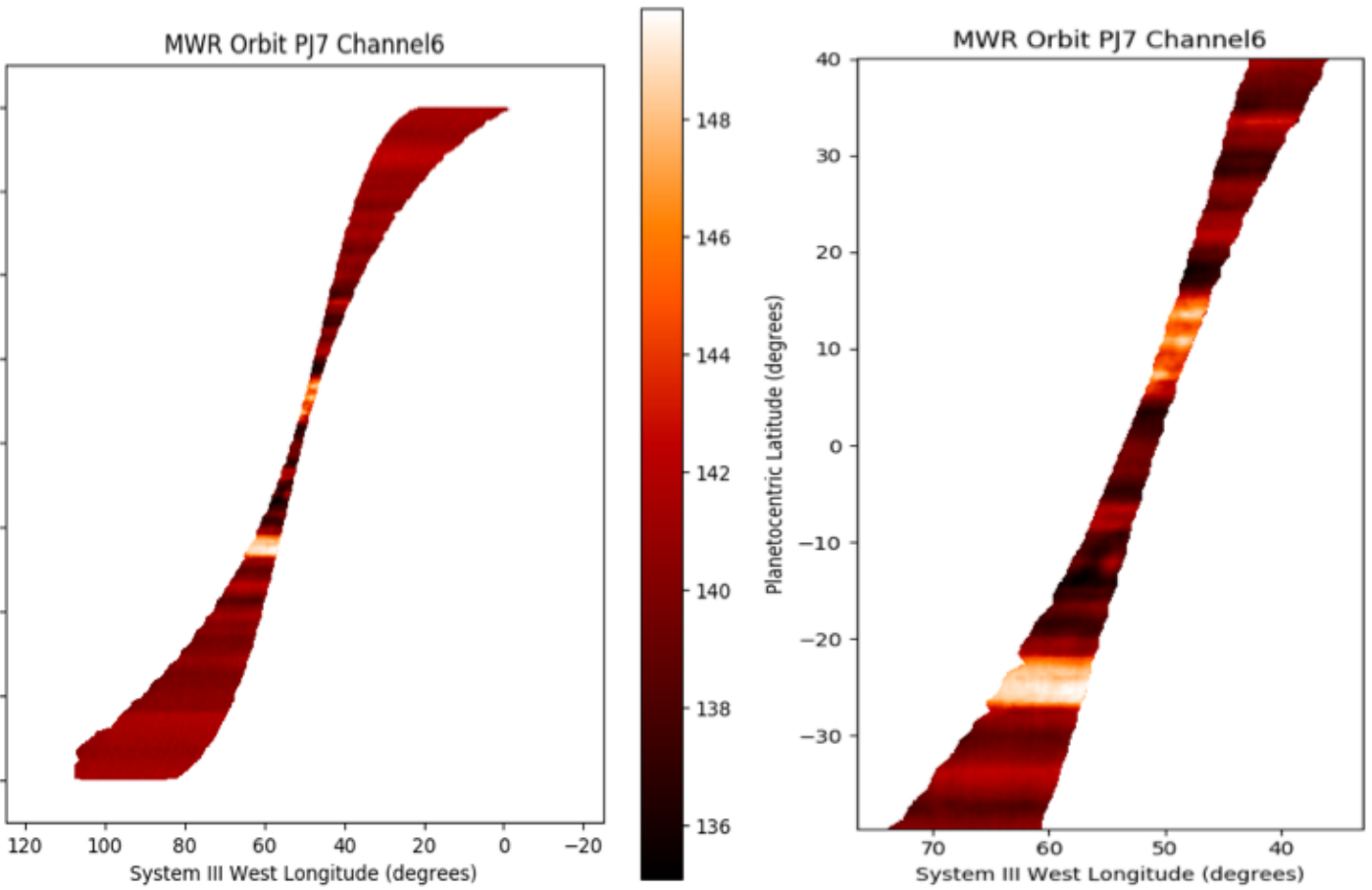
ESS2_634_2020EA001229-f04-z-.png



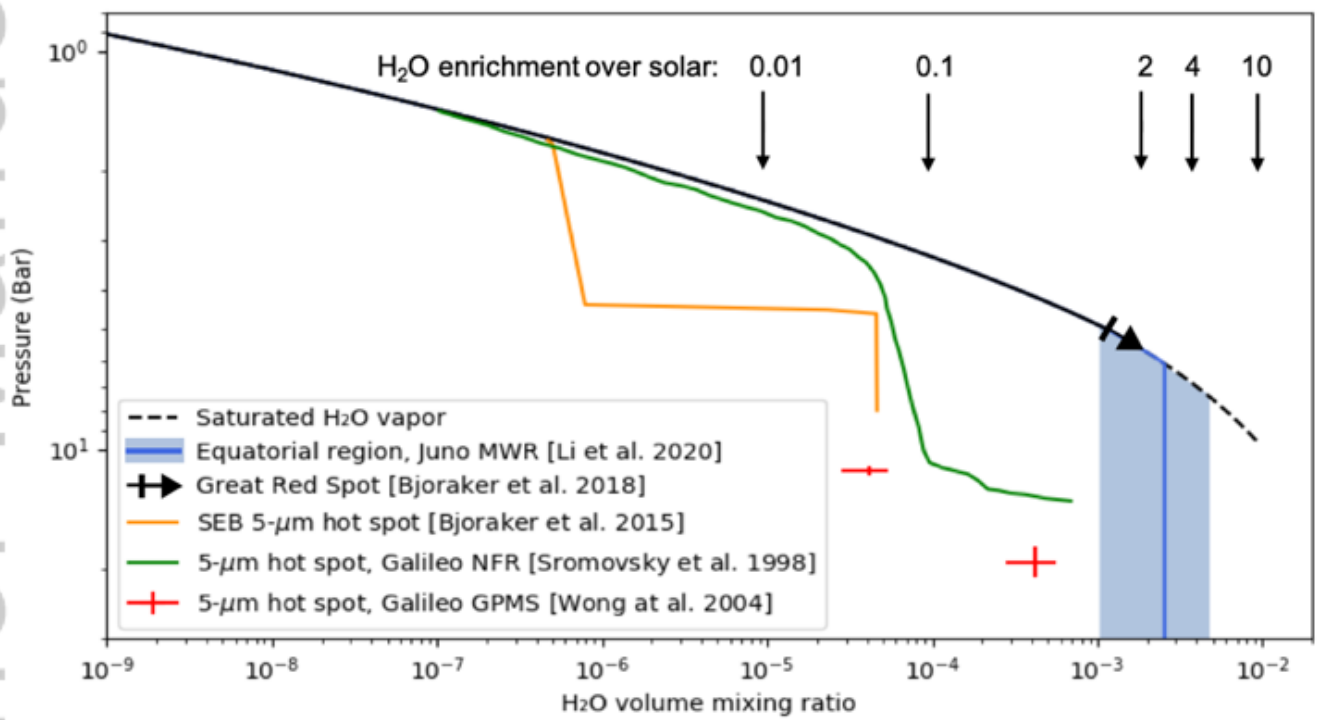
ESS2_634_2020EA001229-f05-z-.png



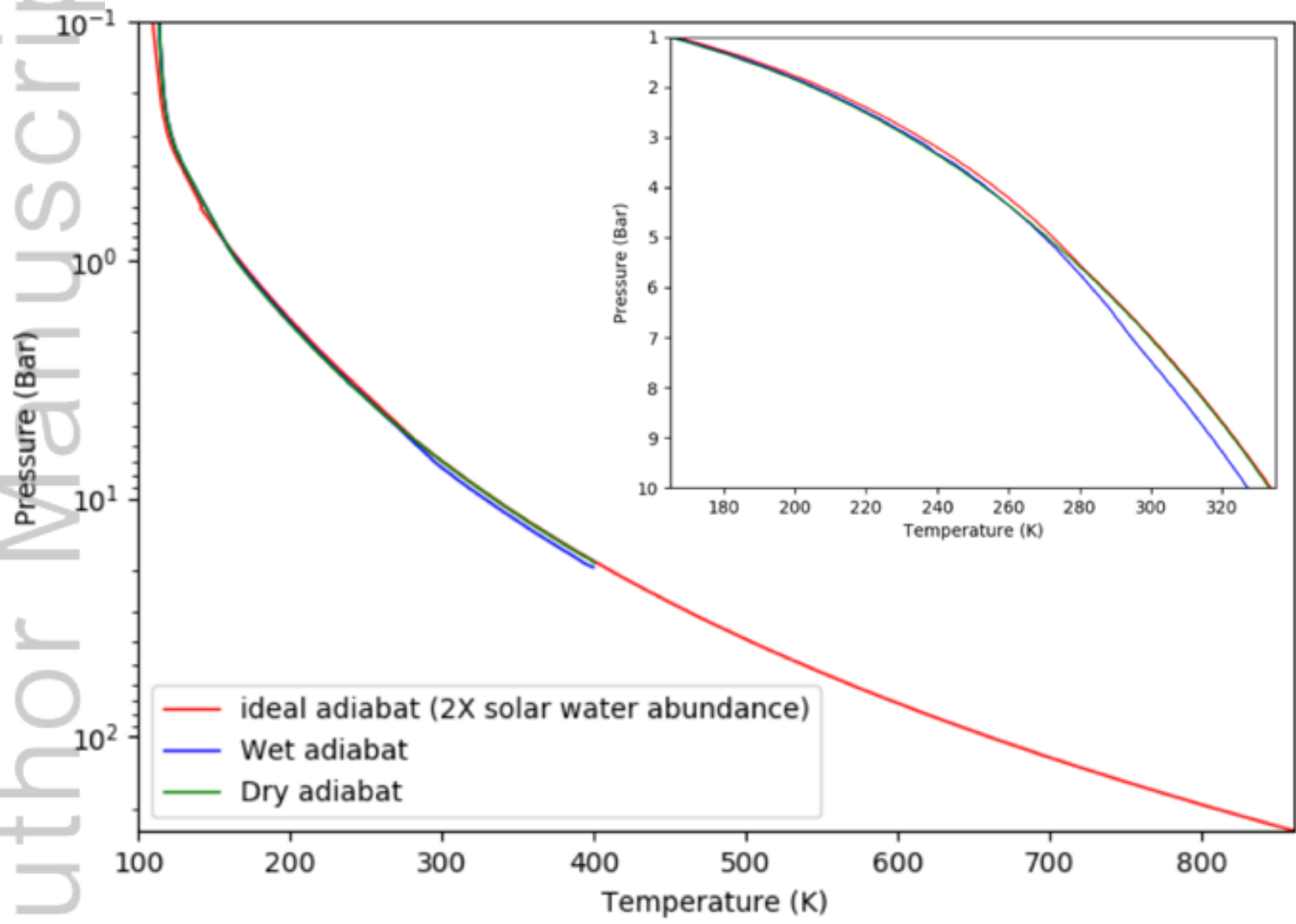
ESS2_634_2020EA001229-f06-z-.png



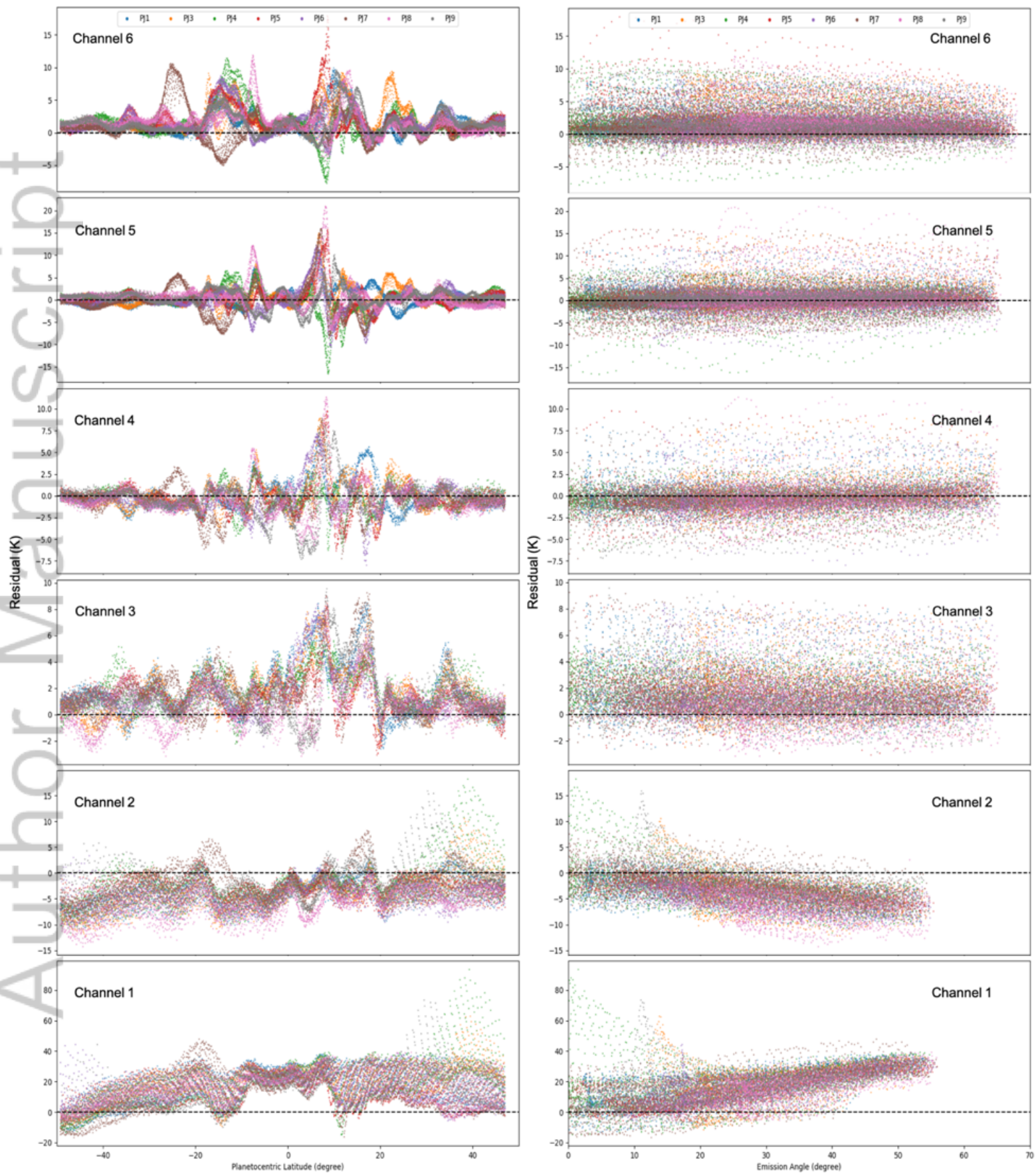
ESS2_634_2020EA001229-f07-z-.png



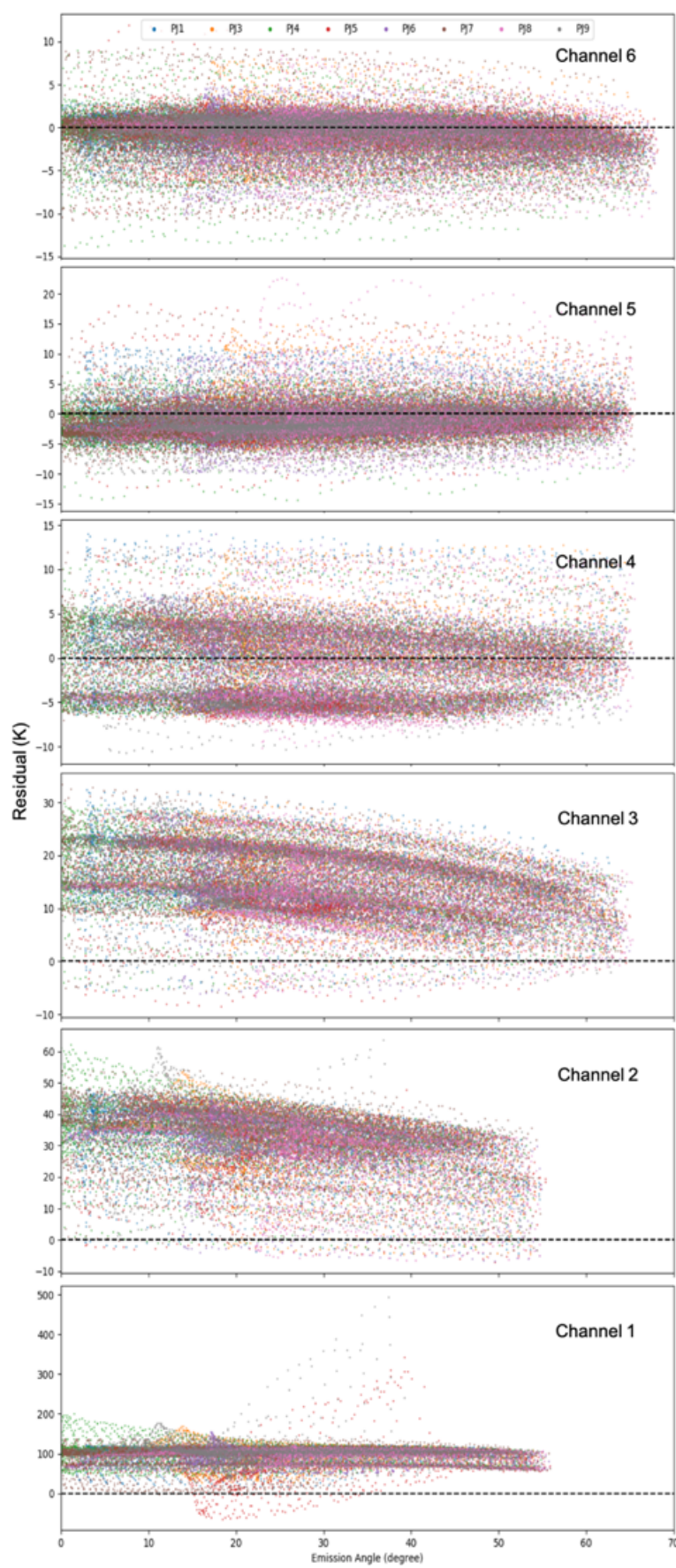
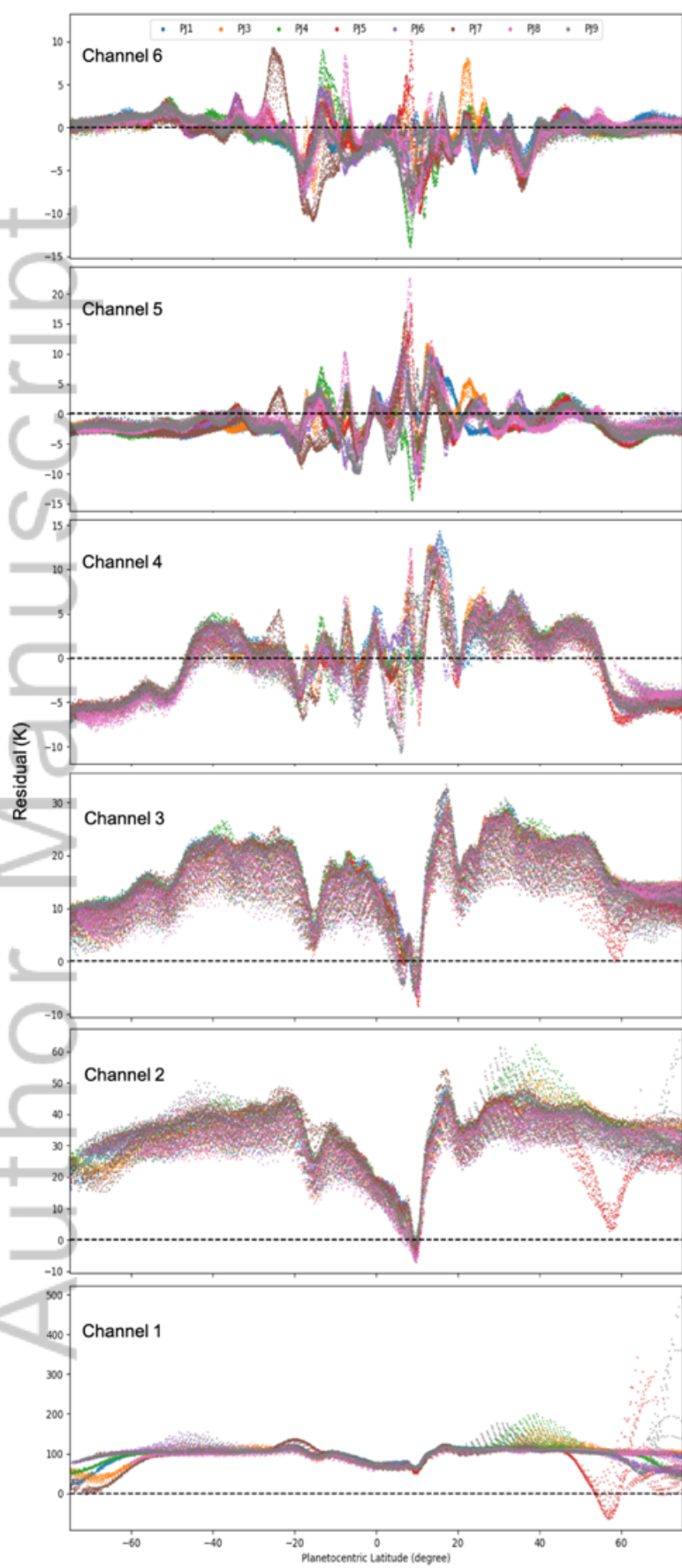
ESS2_634_2020EA001229-f08-z-.png



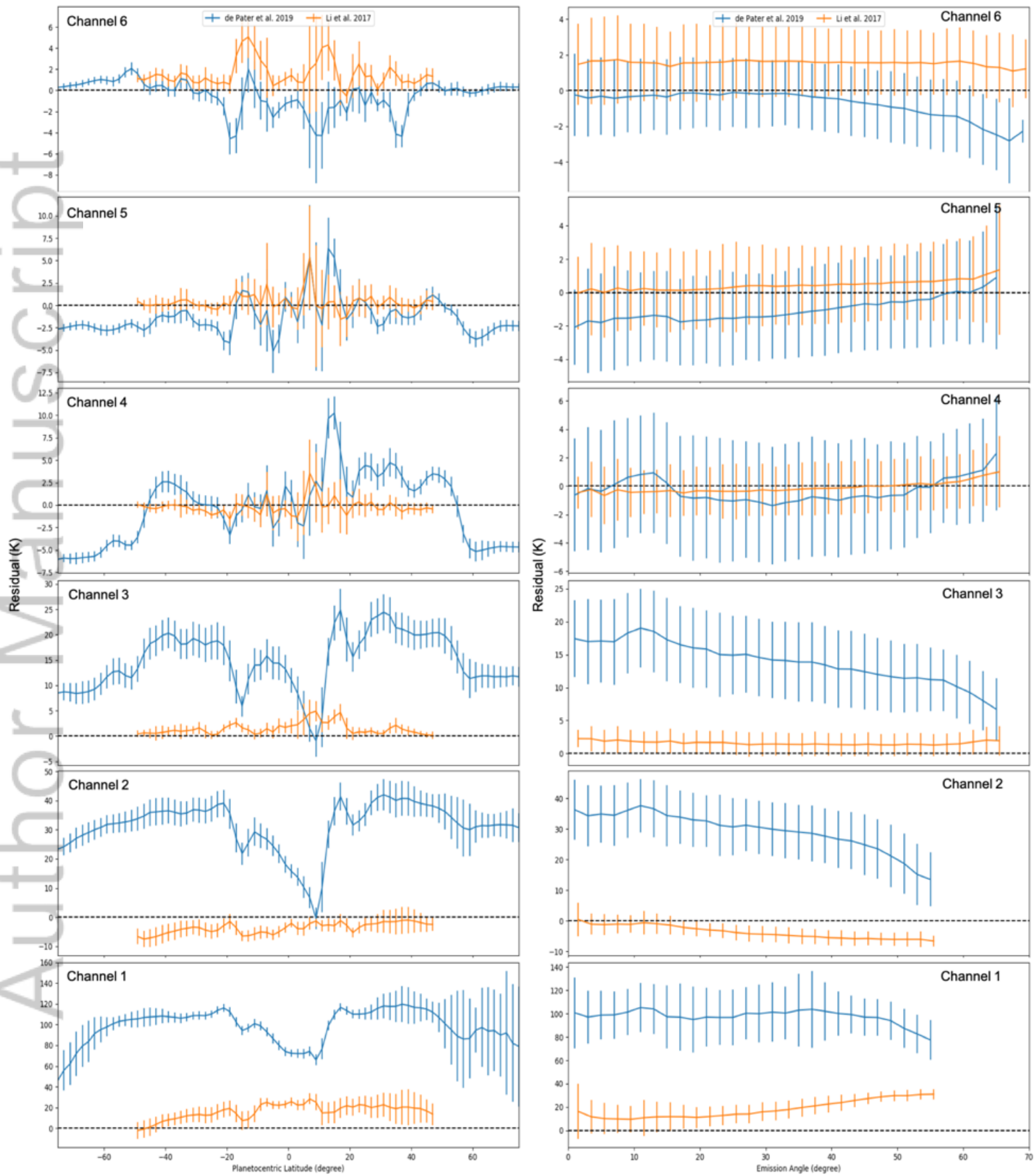
ESS2_634_2020EA001229-f09-z-.png



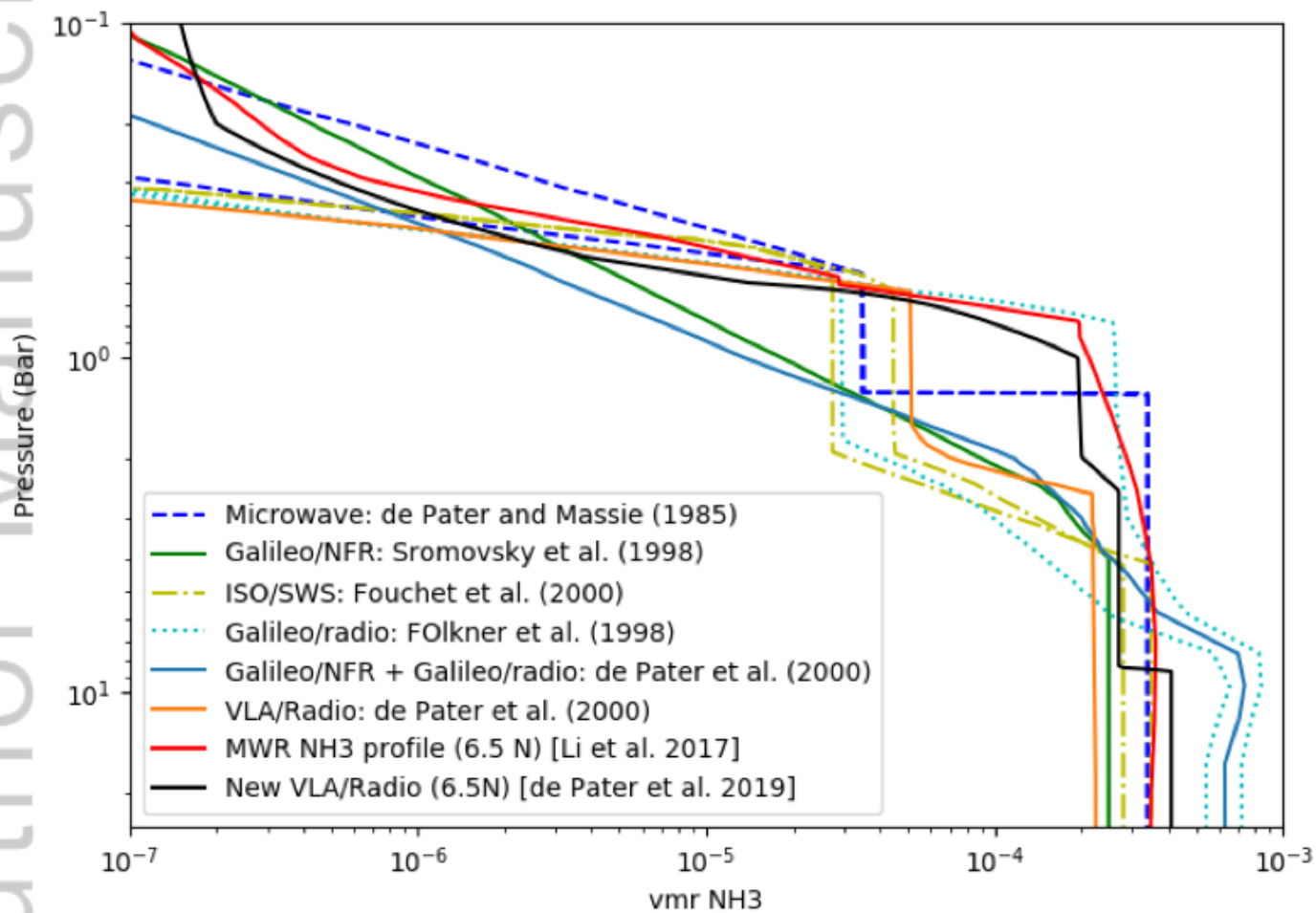
ESS2_634_2020EA001229-f10-z-.png



ESS2_634_2020EA001229-f11-z-.png



ESS2_634_2020EA001229-f12-z-.png



ESS2_634_2020EA001229-f13-z-.png

